



HAL
open science

From deep to shallow fluid reservoirs: evolution of fluid sources during exhumation of the Sierra Almagrera, Betic Cordillera, Spain

Vanessa Dyja, Christian Hibschi, Alexandre Tarantola, Michel Cathelineau, Marie-Christine Boiron, Christian Marignac, Daniele Bartier, Javier Carrillo-Rosúa, Salvador Morales Ruano, Philippe Boulvais

► To cite this version:

Vanessa Dyja, Christian Hibschi, Alexandre Tarantola, Michel Cathelineau, Marie-Christine Boiron, et al.. From deep to shallow fluid reservoirs: evolution of fluid sources during exhumation of the Sierra Almagrera, Betic Cordillera, Spain. *Geofluids*, 2016, 16 (1), pp.103-128. 10.1111/gfl.12139 . insu-01142037

HAL Id: insu-01142037

<https://insu.hal.science/insu-01142037>

Submitted on 21 Apr 2015

HAL is a multi-disciplinary open access archive for the deposit and dissemination of scientific research documents, whether they are published or not. The documents may come from teaching and research institutions in France or abroad, or from public or private research centers.

L'archive ouverte pluridisciplinaire **HAL**, est destinée au dépôt et à la diffusion de documents scientifiques de niveau recherche, publiés ou non, émanant des établissements d'enseignement et de recherche français ou étrangers, des laboratoires publics ou privés.

From deep to shallow fluid reservoirs: evolution of fluid sources during exhumation of the Sierra Almagrera (Betics, Spain)

Journal:	<i>Geofluids</i>
Manuscript ID:	Draft
Manuscript Type:	Original Manuscript
Date Submitted by the Author:	n/a
Complete List of Authors:	Dyja, Vanessa; GeoRessources, Université de Lorraine, CNRS, CREGU, UMR 7359 Hibsch, Christian; GeoRessources, Université de Lorraine, CNRS, CREGU, UMR 7359 Tarantola, Alexandre; GeoRessources, Université de Lorraine, CNRS, CREGU, UMR 7359 Cathelineau, Michel; GeoRessources, Université de Lorraine, CNRS, CREGU, UMR 7359 Boiron, Marie-Christine; GeoRessources, Université de Lorraine, CNRS, CREGU, UMR 7359 Marignac, Christian; GeoRessources, Université de Lorraine, CNRS, CREGU, UMR 7359 Bartier, Danièle; GeoRessources, Université de Lorraine, CNRS, CREGU, UMR 7359 Carrillo-Rosúa, Javier; Universidad de Granada, Facultad de Ciencias, Mineralogía y Petrología Morales, Salvador; Universidad de Granada, Facultad de Ciencias, Mineralogía y Petrología Boulvais, Philippe; Géosciences Rennes, Université de Rennes, UMR CNRS 6118, OSUR,
Key words:	Metamorphic Core Complex, Metamorphic brines, Fluid inclusions, Stable isotopes, Betic Cordillera, Trans-alboran fault

1 1 **From deep to shallow fluid reservoirs: evolution of fluid sources during**
2 2 **exhumation of the Sierra Almagrera (Betics, Spain)**

3
4 3
5 4 Vanessa Dyja ^a, Christian Hibsich ^a, Alexandre Tarantola ^a, Michel Cathelineau ^a, Marie-
6 5 Christine Boiron ^a, Christian Marignac ^a, Danièle Bartier ^a, Javier Carrillo-Rosúa ^b, Salvador
7 6 Morales Ruano ^b and Philippe Boulvais ^c

8 7
9 8 ^a GeoRessources, Université de Lorraine, CNRS, CREGU, UMR 7359, Vandœuvre-lès-
10 9 Nancy, F-54506, France

11 10 ^b Facultad de Ciencias de la Educación, Campus de Cartuja, 18071, Granada, Spain

12 11 ^c Université de Rennes 1, Géosciences Rennes - UMR CNRS 6118, OSUR, 35042 Rennes
13 12 Cedex, France

14 13 **Corresponding Author:**

15 14 E-mail address: vanessa.dyja@univ-lorraine.fr

16 15 Postal address: GeoRessources, UMR 7359, Université de Lorraine, boulevard des Aiguillettes, 54506
17 16 Vandœuvre-lès-Nancy, France

18 17 Tel: +33 3 83 68 47 46

19 18 Fax: +33 3 83 68 47 01

20 19
21 20 **Keywords**

22 21 Metamorphic Core Complex / Metamorphic brines / Fluid inclusions / Stable isotopes / Betic
23 22 Cordillera / Trans-alboran fault

24 23 **Abstract**

25 24 The combination of structural, geochemical and paleotopographic data proves to be an
26 25 efficient tool to understand fluid transfers in the crust. This study discriminates shallow and deep
27 26 fluid reservoirs on both sides of the brittle-ductile transition under an extensional regime, and points
28 27 out the role of major transcurrent fault activity in this paleo-hydrogeological setting.

1
2
3
4
5
6
7
8
9
10
11
12
13
14
15
16
17
18
19
20
21
22
23
24
25
26
27
28
29
30
31
32
33
34
35
36
37
38
39
40
41
42
43
44
45
46
47
48
49
50
51
52
53
54
55
56
57
58
59
60

28 Paleo-fluids trapped in quartz and siderite-barite veins record the transfer of fluids and metal
29 solute species during the Neogene exhumation of the Sierra Almagrera metamorphic belt. Ductile
30 then brittle-ductile extensional quartz veins formed from a deep fluid reservoir, trapping
31 metamorphic secondary brines containing low-density volatile phases derived from the dissolution
32 of Triassic evaporites. During exhumation, low-salinity fluids percolated within the brittle domain,
33 as shown by transgranular fluid inclusion planes affecting previous veins. These observations
34 indicate the opening of the system during Serravalian to early Tortonian times, and provide
35 evidence for the penetration of surficial fluids of meteoric or basinal origin into the upper part of the
36 brittle-ductile transition.

37 During exhumation, synsedimentary transcurrent tectonic processes occurred from Late
38 Tortonian times onwards, while marine conditions prevailed at the Earth's surface. At depth in the
39 brittle domain, quartz veins associated with hematite record a return to high-salinity fluid
40 circulation suggesting an upward transfer fed from the lower reservoir. During the Messinian,
41 ongoing activity of the Trans-Alboran tectono-volcanic trend led to the formation of ore deposits.

42 Reducing fluids led to the formation of siderite and pyrite ores. The subsequent formation of
43 galena and barite may be related to an increase of temperature. The high salinity and Cl/Br ratio of
44 the fluids suggest another source of secondary brine derived from dissolved Messinian evaporites,
45 as corroborated by the $\delta^{34}\text{S}$ signature of barite. This constrains the age of the mineralizing event at
46 around 5.65 Ma, prior to the main Messinian salinity crisis.

47 **1. Introduction**

48 Fluids are vectors of heat and solute species. Migration of fluids is linked to local and
49 regional geology, and permeability is a key factor in controlling fluid flow (Manning & Ingebritsen,
50 1999, Ingebritsen & Manning, 2002). Permeability is a function of time, heterogeneity-anisotropy
51 and scale (Manning & Ingebritsen, 1999). The Sierra Almagrera (southern Spain) is a favourable
52 terrain to evaluate the conditions of fluids migration within the Earth's lithosphere. Because this

1
2 53 area is located in a context of exhumation disturbed by the trans-Alboran transcurrent fault system,
3
4 54 fluid flows can be studied through time across the brittle-ductile transition.

5
6 55 Fluid analysis can focus on the exhumation of metamorphic rocks occurring in wedges
7
8 56 undergoing active thickening, owing to the intense erosion of the hanging-wall overlying thrust
9
10 57 systems (Menzies *et al.*, 2014). Within Basin and Range type provinces, studies of fluids can also
11
12 58 elucidate the exhumation of rocks from the footwall during thinning processes as revealed by the
13
14 59 presence of crustal detachments associated with low-angle and high-angle normal faults (Wernicke
15
16 60 & Burchfiel, 1982, Lister & Davis, 1989, Vanderhaeghe & Teyssier, 2001). In both geological
17
18 61 settings, the location of the brittle-ductile transition plays a major role. In extensional settings, this
19
20 62 rheological transition may localize detachment and decollement layers where normal faults are
21
22 63 generally rooted. There is currently much debate about the hydrogeological role of the brittle-
23
24 64 ductile transition. The rheological change occurring at this transition may separate a deep reservoir,
25
26 65 which is accessible to metamorphic and/or magmatic and mantle fluids confined under lithostatic
27
28 66 conditions, from a shallower reservoir accessible to surficial fluids (meteoric, marine or basinal)
29
30 67 circulating under lithostatic to hydrostatic conditions (Morrison & Anderson, 1998, Famin &
31
32 68 Nakashima, 2004). These two reservoirs may interact through tectonic and magmatic processes.
33
34 69 Surficial fluids may reach the upper part of the deeper reservoir under contractional regimes
35
36 70 (Menzies *et al.*, 2014) as well as under extensional regimes (Mulch *et al.*, 2004, Famin *et al.*, 2005,
37
38 71 Siebenaller *et al.*, 2013). Alternatively, deeper fluids may access the upper brittle crust and mix
39
40 72 with fluids closer to the Earth's surface (Boiron *et al.*, 2003), a process which may also be triggered
41
42 73 by magma ascent. Such fluid circulation events are commonly associated with hydrothermal
43
44 74 processes (metasomatism and mineralization) (Beaudoin, 1994), and it is then necessary to decipher
45
46 75 the role played by the different reservoirs and fluids during the tectonic and magmatic events.
47
48
49
50
51

52
53 76 The convergence between Africa and Europe resulted in a complex geotectonic history with
54
55 77 subduction of upper continental crust (Eocene to Middle Miocene), followed by extensional
56
57 78 tectonics. This early extension triggered the exhumation of metamorphic cores in the internal zones
58
59
60

1
2 79 of the Betic cordillera during the Miocene (between 18 to 14 Ma: Gomez-Pugnaire *et al.* (2004),
3
4 80 Platt *et al.* (2006) and Gomez-Pugnaire (2012), and possibly even earlier (Augier *et al.*, 2005b).
5
6 81 Further exhumation has occurred under compressional regimes since the late Miocene due to
7
8 82 erosional processes affecting the uplifting metamorphic cores. The different mountain ranges have
9
10 83 been also partly dissected by a major transcurrent fault system, which has led to the formation of
11
12 84 synsedimentary continental to marine basins (Weijermars, 1985, Booth-Rea *et al.*, 2003).
13
14 85 Volcanism occurred later in the evolution of the Betics, reflecting mantle and crust processes as
15
16 86 well as mantle-crust interactions at depth (e.g. Benito *et al.* (1999); Turner *et al.* (1999); Duggen *et*
17
18 87 *al.* (2004)). A major erosional event allowed the uplift of ranges during the Messinian salinity crisis.
19
20 88 Deposition of evaporites in the central Mediterranean Sea and incision features affected the
21
22 89 bordering slopes. Prior to the main sea-level drop (5.60-5.46 Ma), a first stage of deposition of
23
24 90 evaporites with controversial ages (7.20 Ma / 5.96-5.67 Ma) has been recorded in some basins of
25
26 91 the Betics (Fortuna, Lorca, Guadix-Baza, Granada and Sorbas) (Clauzon, 1980, Gautier *et al.*, 1994,
27
28 92 Garcés *et al.*, 1998, Rouchy *et al.*, 1998, Krijgsman *et al.*, 1999, Seidenkrantz *et al.*, 2000,
29
30 93 Krijgsman *et al.*, 2000, Gargani *et al.*, 2008, Bourillot *et al.*, 2009, Omodeo Salé *et al.*, 2012).
31
32
33
34

35 94 The Sierra Almagrera metamorphic core exhibits a sequence of quartz vein formation. A
36
37 95 series of siderite and barite base metal-bearing ore veins, as well as quartz and carbonate barren
38
39 96 veins in the brittle domain, are associated with the transcurrent tectonics. Study of the different
40
41 97 fluids trapped as inclusions in this vein sequence allows the characterization of the deep reservoir
42
43 98 fluids in equilibrium with the rocks during the ductile stage and the evolution of the fluids within
44
45 99 the same reservoir during its exhumation towards exposure at the present day. This reservoir was
46
47 100 subject to different deformation styles, from ductile to brittle, and records the Neogene evolution of
48
49 101 this part of the Betic orogenic wedge.
50
51

52 102 In this study, we combine structural, paleogeographical and geochemical data to propose a
53
54 103 scenario of hydrogeological evolution during exhumation across the brittle-ductile transition in the
55
56 104 Sierra Almagrera. In addition, we discuss the hydrogeological influence of the brittle ductile
57
58
59
60

1
2 105 transition on the lower and upper crustal reservoirs during the Miocene extensional tectonics, the
3
4 106 effect of transcurrent deformation on the hydrogeological configuration, the possible fluid sources
5
6 107 at the various stages of this evolution and the timing of mineralizations in the region.
7
8

9 108 **2. Geological context**

10 111 **2.1. The Betic Cordillera (SE Spain)**

11 112 The Betic Cordillera results from the convergence between the Africa and Eurasia plates
12 113 since the Eocene, and forms an alpine tectonic wedge reaching a thickness of about 60 km (Platt &
13 114 Vissers, 1989, Lonergan & White, 1997, Platt, 2007, Jolivet et al., 2008). The internal Alboran
14 115 domain can be divided into three main tectono-metamorphic nappes, from bottom to top (Figure 1):
15 116 (i) the Nevado-Filábride nappe, itself divided into three sub-units from bottom to top: Ragua (not
16 117 represented on Figure 1, to the W), Calar-Alto and Bedar-Macael (De Jong, 1991, Martínez-
17 118 Martínez et al., 2002), (ii) the Alpujarride nappe, and (iii) the Malaguide nappes (Egeler & Simon,
18 119 1969). In addition to isostatic uplift, these units were also exhumed due to tectonic unroofing
19 120 (Lonergan & Mange-Rajetzky, 1994). The associated WSW-ENE-striking tectonic extension
20 121 related to exhumation of the metamorphic continental crust is supposed to have resulted from partial
21 122 or complete removal of the lithospheric mantle (Platt & Vissers, 1989). Arguments have also been
22 123 put forward for other mechanisms, such as subduction zone rollback (Lonergan & White, 1997,
23 124 Bezada et al., 2013). The contacts observed between structural units exhibiting different degrees of
24 125 metamorphism are attributed to major detachment faults (Figure 1-a): (1) The Malaguide-
25 126 Alpujarride contact: unmetamorphosed Malaguide lithologies overlie the medium-pressure
26 127 medium-temperature metamorphic rocks of the Alpujarride nappe (Sierra Estancias, Figure 1-a), (2)
27 128 The Filabres major detachment: higher grade Nevado-Filábride metamorphic rocks, which were
28 129 exhumed during the Miocene, lie beneath the Alpujarride nappes. Ductile shearing related to this
29 130 exhumation affected the footwall and currently shows a transport direction top towards WSW to
30 131 SW (Crespo-Blanc et al., 1994, Martínez-Martínez & Azañón, 2002, Platt, 2007). According to the
31 132 extensional tectonics expressed in the ductile fabrics, the metamorphic nappes reached the brittle
32 133
33
34
35
36
37
38
39
40
41
42
43
44
45
46
47
48
49
50
51
52
53
54
55
56
57
58
59
60

1
2 131 domain during the ongoing exhumation. From the late Miocene, exhumation was mainly the result
3
4 132 of erosion since both the metamorphic cores and the sedimentary cover were affected by regional
5
6 133 compressional and local transcurrent tectonics. The Trans-Alboran transcurrent fault system
7
8 134 generated domains with both releasing and restraining deformation, which created juxtaposed zones
9
10 135 with opposite vertical motions (subsidence and uplift). The ranges (sierras) were separated by
11
12 136 basins either filled by continental or marine sediments according to time and location. This major
13
14 137 tectono-volcanic trend can be followed off-shore to the other side of the Mediterranean in Morocco
15
16 138 (Hernandez et al., 1987).

17
18
19 139 The volcanism linked to lithospheric thinning shows a gradual transition and great
20
21 140 geochemical diversity. The age of this volcanism varies from 34 Ma (tholeiitic dykes in Malaga
22
23 141 province) to 2 Ma (alkali basalts in Murcia province). There is a gap between the oldest volcanic
24
25 142 events in Malaga and the main magmatic activity in SE Spain and the Alboran Basin, which took
26
27 143 place between 12.6 and 7.5 Ma with tholeiitic and calc-alkaline affinities (Bellon *et al.*, 1983). Very
28
29 144 locally in the Sierra Cabrera, Miocene plutonism is recorded related to the retrograde
30
31 145 metamorphism and associated ductile deformation (Westra, 1969, Bolze *et al.*, 1986). Since the
32
33 146 reappearance of volcanism during the Serravalian, other episodes of magmatic activity occurred
34
35 147 inland in SE Spain mainly between 10 and 6.2 Ma, showing high-K calc-alkaline, shoshonitic and
36
37 148 ultrapotassic affinities (Bellon *et al.*, 1983, Turner *et al.*, 1999, Zeck *et al.*, 2000, Duggen *et al.*,
38
39 149 2004, Duggen *et al.*, 2005, Cesare *et al.*, 2009). Heterogeneous sources and various processes are
40
41 150 implied in the magma genesis, including: (i) various degrees of partial melting, (ii) metasomatism
42
43 151 (i.e. oceanic and continental crust, sediments), (iii) anatexis of crustal metasedimentary basement
44
45 152 (Benito *et al.*, 1999, Duggen *et al.*, 2004, Duggen *et al.*, 2005, Prelevic *et al.*, 2008, Álvarez-Valero
46
47 153 & Kriegsman, 2008, Conticelli *et al.*, 2009).

48
49
50 154 The Neogene evolution of the Betics is associated with a series of base and precious metal-
51
52 155 bearing hydrothermal ore systems developed mainly in the calc-alkaline volcanic rocks of the Cabo
53
54 156 de Gata range, but also in sedimentary and metamorphic basement lithologies (Figure 1).

1 157 Epithermal ore deposits are hosted by intermediate to acid volcanics ranging in age from 12 to 10
2
3
4 158 Ma; these deposits are found in a number of different mining districts, for example, Zn-Pb-Cu(-Ag-
5
6 159 Au) at San José (Demoustier *et al.*, 1998, Esteban-Arispe *et al.*, 2009), Au(-Cu-Te-Sn) at
7
8 160 Rodalquilar (Arribas *et al.*, 1995) and Cu-Au-Ag at Carboneras (Morales Ruano *et al.*, 2000,
9
10 161 Carrillo-Rosúa *et al.*, 2009). Ba-Ag mineralizations are found in sedimentary rocks, close to high-K
11
12 162 calc-alkaline and shoshonitic volcanics within the Vera Basin (Alvado, 1986, Martínez-Frías,
13
14 163 1998). Certain ore deposits are hosted by metamorphic rocks, including the occurrences of Pb-Zn-
15
16 164 Fe-Cu (Al) at Cartagena (Graeser & Friedrich, 1970, Oen *et al.*, 1975, Arribas *et al.*, 1983) and Pb-
17
18 165 Zn-Ag-Fe at Sierra Almagrera and Sierra Aguilon (Martinez Frias *et al.*, 1989, Morales Ruano *et*
19
20 166 *al.*, 1993). Samples from the Sierra Almagrera mining district allow us to reconstruct the fluid
21
22 167 history described below.
23
24
25

26 168 **2.2. Geology of the Sierra Almagrera (Figure 1-b)**

27
28
29 169 The metamorphic range of the Sierra Almagrera exposes a Nevado Filabres unit largely
30
31 170 composed of graphitic quartz-rich chloritoid-schists (Booth-Rea *et al.*, 2004) and quartzites.
32
33 171 Locally, carbonates and gypsum are found north of the Sierra Almagrera within an Alpujarride unit
34
35 172 (Álvarez & Aldaya, 1985). The present-day geomorphology of the Sierra Almagrera mainly results
36
37 173 from sinistral strike-slip faulting in the area that generated several fault segments at various scales.
38
39 174 The Palomares Fault Zone results in an approximately 16 km North-South trending left-lateral
40
41 175 relative displacement (Booth-Rea *et al.*, 2004). This transcurrent faulting may have started during
42
43 176 the late Tortonian (around 7.2 Ma), but was mainly active during the Messinian. The evolution of
44
45 177 this faulting associated with a vertical component (oblique faulting) caused the recent uplift, thus
46
47 178 leading to erosion and exhumation of the Sierra Almagrera during the Plio-Quaternary. The
48
49 179 southern segments of the Palomares Fault Zone dip towards the West. Their transtensional activity
50
51 180 favoured the subsidence of the western block. By contrast, the northern segments, which are
52
53 181 dipping towards the ESE, are related to a sinistral restraining bend that favoured the uplift of the
54
55 182 Sierra Almagrera mountain ranges located to the East of the zone (Booth-Rea *et al.*, 2004). In the
56
57
58
59
60

1
2 183 studied area, small bodies of high-K calc-alkaline to shoshonitic rhyodacites (Lopez Ruiz &
3
4 184 Rodriguez Badiola, 1980, Benito *et al.*, 1999) are encountered along the transcurrent fault system.
5
6 185 Regional ages determined on this volcanic suite are between 11.9 and 6.2 Ma (Duggen *et al.*, 2004).
7
8 186 Less abundant lamproites from the ultrapotassic series (Lopez Ruiz & Rodriguez Badiola, 1980),
9
10 187 dated at between 8.4 and 6.4 Ma (Prelevic *et al.*, 2008), crop out within the Vera basin to the south
11
12 188 of Sierra Almagrera (Figure 1-b).

13
14
15 189 Mineralizations in the Sierra Almagrera are found in veins within the metamorphic rocks of
16
17 190 the currently uplifted metamorphic range (Figure 1-b). In the present study, this formerly exploited
18
19 191 area is referred to as the Sierra Almagrera mining district. While some mineralised veins are
20
21 192 exposed at outcrop in the Sierra, the sulphides are frequently oxidized. Non-altered veins can still
22
23 193 be sampled along the E-W striking horizontal gallery at El Arteal. Subvertical fractures filled by
24
25 194 siderite, barite, hematite and ore minerals crosscut the metamorphic fabric of graphitic schists and
26
27 195 quartz veins transposed or partly transposed within the main rock foliation. Our study shows that
28
29 196 the mineralised fractures are arranged in two main clusters striking N160°-N180° and N120°-N130°
30
31 197 (Figure 1-c).

32
33
34
35 198 The area located within the Palomares Fault Zone (hanging-wall) is referred to here as “the
36
37 199 subsident area”. Locally, mineralizations can be found within the Messinian sediments (Las
38
39 200 Herrerias). The ore consists of barite veins, with native Ag and base-metal sulphides in very small
40
41 201 amounts (Alvado, 1986, Martínez-Frías, 1998, Carrillo-Rosúa *et al.*, 2002, 2003).

42 43 44 202 **3. Methods**

45 46 47 203 **3.1. Fluid inclusion investigations**

48 49 50 204 **3.1.1 Fluid inclusion petrography**

51
52
53 205 Double-polished 150-200- μm -thick sections were prepared for microscopic and
54
55 206 microthermometric observations of mineralized veins of quartz, siderite, barite and calcite. The
56
57 207 sections were oriented (using azimuth convention) to determine present-day strike and dip of fluid
58
59
60

1
2 208 inclusion planes. Isolated fluid inclusions or clusters are interpreted as primary. Intragranular fluid
3
4 209 inclusion planes are found within single grains in microcracks that do not cross-cut grain boundaries
5
6 210 (Van Den Kerkhof & Hein, 2001). Transgranular fluid inclusion planes result from healing of
7
8 211 former open cracks (Krantz, 1983, Boullier, 1999, Lespinasse, 1999, Lespinasse *et al.*, 2005) as
9
10 212 rocks undergo brittle deformation. Systematic measurements of the fluid inclusion planes were
11
12 213 carried out on each section using an ANIMA interactive videographic image analyzer (Lespinasse
13
14 214 *et al.*, 2005). The plunge and dip directions of the fluid inclusion planes are represented on equal-
15
16 215 area lower-hemisphere stereograms using Stereonet® software.

20 216 **3.1.2 Microthermometry**

21
22 217 The phase transitions of the fluid inclusions were characterised between $-170\text{ }^{\circ}\text{C}$ and $+600\text{ }^{\circ}\text{C}$
23
24 218 using a LINKAM MDS 600 heating-freezing stage mounted on an Olympus microscope, calibrated
25
26 219 using CO_2 and H_2O synthetic and natural alpine fluid inclusions. The accuracy of measurements
27
28 220 varies from $\pm 0.2\text{ }^{\circ}\text{C}$ at low temperature (experiments at $0.5\text{-}1\text{ }^{\circ}\text{C}/\text{min}$) to $\pm 2\text{ }^{\circ}\text{C}$ at high temperature
29
30 221 (experiments at $1\text{-}5\text{ }^{\circ}\text{C}/\text{min}$). Table 1 reports the abbreviations of terms and the phase transition
31
32 222 temperatures observed during microthermometric experiments. For barite and calcite, the high-
33
34 223 temperature transitions were studied first to prevent leakage of fluid inclusions during ice formation
35
36 224 on cooling. Photographs of fluid inclusions after each measurement were compared with the
37
38 225 original picture to evaluate any leakage.

43 226 **3.1.3 Raman microspectroscopy**

44
45 227 Raman analysis of fluid inclusions was performed with a LabRAM microspectrometer
46
47 228 (Horiba Jobin Yvon, at GeoRessources, Vandœuvre-lès-Nancy, France) equipped with a 1800
48
49 229 gr. mm^{-1} grating and a $\times 80$ Olympus objective. The exciting radiation was provided by the 514.5 nm
50
51 230 line of an Ar^+ laser (Stabilite 2017, Newport Corp., Spectra Physics) at a power of 400 mW . The
52
53 231 signal-to-noise ratio was optimized by adjusting acquisition time and accumulation number. The
54
55 232 quantitative analysis of the gas phase was performed using a specific calibration of the laboratory.
56
57 233 Results are given as mol% relative to the volatile phase.
58
59
60

234 **3.1.4 *P-V-T-X calculation of fluid inclusions***

235 In this study, we use microthermometric data associated with mole fractions of the different
236 gas species obtained by Raman spectroscopy to reconstruct the *P-V-T-X* evolution of fluid
237 inclusions. The salinities of aqueous fluid are calculated using the final melting temperature of ice
238 when gases are not present in sufficient amounts to form gas hydrates (Bodnar, 2003). In this case,
239 the isochore is a function of the homogenization temperature at a given salinity, and the empirical
240 equation of state of Zhang and Frantz (1987) is used within a *P-T* domain of validity of *T*: 180-700
241 °C and *P*: 0.1-300 MPa.

242 The salinities of aqueous carbonic fluids and molar volumes (V_m) of the volatile phase are
243 calculated using the program ICE and the dissociation temperature of clathrate (Bakker, 1997,
244 2003) when gases are present in significant amounts to allow the formation of gas hydrates. The
245 isochores are calculated using the program ISOC (Bakker, 1997, 2003) and the equation of state
246 (Bowers & Helgeson, 1983) revised by Bakker (1999) for the system H₂O-CO₂-CH₄-N₂-NaCl, with
247 a *P-T* domain of validity of *T*: 350-600 °C and *P*: 50-200 MPa.

248 **3.1.5 *Crush-leach analysis for halogen chemistry***

249 Because the halogens display a conservative behaviour in solution, and remain relatively
250 unaffected by fluid-rock interactions (Banks *et al.*, 1991), the signature of the elements Cl and Br in
251 a fluid can be used to characterize its source (Böhlke & Irwin, 1992).

252 Bulk crush-leach analyses were performed to extract and analyse fluids hosted in quartz,
253 barite and siderite. Samples were prepared according to the methodology of Bottrell *et al.* (1988).
254 The amount of sample crushed was between 0.5 and 1.0 g. Analysis of the anions F, Cl, Br, I and
255 SO₄ was performed by ion chromatography using a ICS 3000 Dionex system with a AS20 column
256 at the LIEC laboratory (Nancy, France). Br was also analysed by LA-ICPMS in a series of
257 representative fluid inclusions using the procedure described by Leisen *et al.* (2012a).

258 **3.1.6 *Laser Ablation ICP-MS***

1
2 259 This technique allows direct ablation of individual fluid inclusions within the host mineral,
3
4 260 represented in the present study by quartz, siderite and barite. The LA-ICP-MS instrument
5
6 261 (GeoRessources laboratory, Vandœuvre-lès-Nancy, France) comprises a GeoLas excimer laser
7
8 262 (ArF, 193 nm, Microlas, Göttingen Germany) and an Agilent 7500c quadrupole ICP-MS equipped
9
10 263 with an octopole reaction-cell using H₂ gas, and a collision-cell using He gas. The laser beam is
11
12 264 focused onto the sample within an ablation cell with a Schwarzschild objective (magnification x25)
13
14 265 linked with a CCD camera. Synthetic glass provided by the National Institute of Standards and
15
16 266 Technology (NIST) is used for calibration of the different analysed elements and respective masses
17
18 267 (200 pulses at 5 Hz). The design as an optical imaging system allows the use of different crater
19
20 268 diameters (24, 32 or 60 µm) at constant energy density on the sample, by adjusting an aperture in
21
22 269 the laser beam path. Na, K, Mg, Ba, Sr, Mn, Li, Fe, Cu and Zn are analysed here. Concentrations
23
24 270 are calculated according to Leisen *et al.* (2012b).

271 **3.2. Raman spectroscopy of carbonaceous materials**

272 The Raman Spectrum of Carbonaceous Material (RSCM) has been calibrated as a
273 geothermometer in the range 330-640 °C (Beyssac *et al.*, (2002, 2004)). The RSCM displays one
274 graphite band (G band) and several defect-activated bands (D1 and D2 bands) between 1100 and
275 1800 cm⁻¹ (Beyssac & Lazzeri, 2012), whose intensities decrease with increasing metamorphic
276 grade. Raman analysis of graphite-bearing schists was performed on thin sections oriented
277 perpendicular to the foliation and parallel to the lineation by focusing the laser beam beneath a
278 transparent crystal to avoid the effect of amorphization due to polishing. The Raman spectrometer
279 used in this study is a LabRAM HR instrument (Horiba Jobin Yvon) (GeoRessources, Vandœuvre-
280 lès-Nancy, France) equipped with a 600 gr.mm⁻¹ grating and a ×100 objective (Olympus). The
281 excitation beam is provided by an Ar⁺ laser (Stabilite 2017, Newport Corp., Spectra Physics) at
282 457.9 nm. Laser power is reduced to avoid heating the samples, using optical filters of various
283 optical densities, and was always lower than 5 mW. The acquisition time is 15 seconds, with each
284 measurement repeated 6 times. 10 to 15 spectra are recorded for each sample for statistical

1
2 285 purposes. Peak fitting is performed using the Peak Analyser of the OriginPro 8.5.1 software. The
3
4 286 following expression (Beysac *et al.*, 2002) is used to derive peak temperature conditions: $T(^{\circ}\text{C}) = -$
5
6 287 $445R_2 + 641$, with R_2 (peak area ratio) = $(D_1/(G+D_1+D_2))$.
7

8 9 288 **3.3. Stable isotopes**

10 11 289 **3.3.1 $\delta^{18}\text{O}$ and $\delta^{13}\text{C}$ of siderite**

12
13
14 290 15 to 20 mg of siderite were reacted at 70 °C with H_3PO_4 for 15 days (Scheppard &
15
16 291 Schwarcz, 1970). Isotopic ratios were measured using a modified VG 602D mass spectrometer at
17
18 292 the CRPG laboratory (Vandœuvre-lès-Nancy, France), and the results are reported using
19
20 293 conventional $\delta^{18}\text{O}$ (V-SMOW) and $\delta^{13}\text{C}$ (V-PDB) notations. The analytical reproducibility is ± 0.1
21
22 294 ‰ for $\delta^{18}\text{O}$ and $\delta^{13}\text{C}$.
23
24

25 26 295 **3.3.2 $\delta^{18}\text{O}$ of quartz**

27
28 296 6.5 to 7.5 mg of quartz (same grains as those used for fluid inclusion analyses) were analysed
29
30 297 using the conventional fluorination method (Clayton & Mayeda, (1963). The measurements were
31
32 298 carried out with a VG SIRA 10 triple-collector instrument at the University of Rennes 1 (France).
33
34 299 The analytical reproducibility (estimated from duplicates performed on different Ni fluorination
35
36 300 tubes) is $\pm 0.2\%$.
37
38
39

40 41 301 **3.3.3 $\delta^{34}\text{S}$ of sulphides and sulphates**

42
43 302 Sulphur isotope compositions were measured following the method of Giesemann *et al.*
44
45 303 (1994) at the CRPG laboratory (Vandœuvre-lès-Nancy, France) by EA-IRMS (Elemental Analyser-
46
47 304 Isotopic Ratio Mass Spectrometer). $\delta^{34}\text{S}$ was measured with a GV Instruments Isoprime mass
48
49 305 spectrometer coupled in continuous-flow mode to a EuroVector elemental analyser. Results are
50
51 306 reported using conventional $\delta^{34}\text{S}$ (CDT). No inter-sample memory effect was observed. Linearity of
52
53 307 the mass spectrometer and reproducibility of the analysis were checked using CRPG internal
54
55 308 reference materials. The analytical reproducibility obtained on the barium sulphate reference
56
57 309 material used at CRPG is lower than 0.3 ‰.
58
59
60

3.3.4 δD of white micas

2 to 3 mg of powdered host-rock were analysed for the isotopic composition of hydrogen-bearing minerals, mainly phengite. δD was measured with a GV Instruments Isoprime mass spectrometer coupled in continuous-flow mode to a EuroVector elemental analyser. No inter-sample memory effect can be observed. Linearity of the mass spectrometer and reproducibility of the analysis were checked using CRPG internal reference materials with an analytical reproducibility lower than 0.3‰.

3.3.5 δD of fluid inclusions

Fluids trapped in quartz, barite and siderite crystals were extracted for isotopic analyses by crushing under vacuum. Aliquots of 1.0 to 5.1 g of mm-sized grains were loaded into steel tubes and degassed overnight at 120 °C under vacuum to release any water adsorbed at the mineral surface (Dublyansky & Spötl, 2009). Preliminary tests conducted under the microthermometric heating stage showed no decrepitation or stretching of the studied fluid inclusions at temperatures below 200 °C. H₂O was separated cryogenically from other gases and reduced to H₂ in a uranium reactor at 800 °C. D/H ratio of H₂ was determined using a dual-inlet VG Micromass 602D mass spectrometer at the CRPG laboratory (Vandœuvre-lès-Nancy, France). External reproducibility of D/H measurements was estimated to be lower than 3 ‰ by normalizing raw data to the V-SMOW-SLAP scale. Two CRPG water standards were analysed along with each weekly batch of water samples obtained from the fluid inclusions.

To avoid any memory effect on D/H ratios within the uranium reactor, samples were systematically duplicated. For each duplicate, δD values from the first extraction are discarded since they could be affected by this memory effect.

For quartz containing primary inclusions, $\delta^{18}\text{O}_{\text{fluid}}$ was calculated from $\delta^{18}\text{O}_{\text{quartz}}$ using the quartz-water fractionation equation of Zheng (1993) at a given temperature.

335 4. Results

336 4.1. Characteristics of the host-rock

337 All sampled veins are hosted in schists composed of phengite, quartz, graphite and rutile.
338 Although not observed in this study, biotite and garnet have also been described in these rocks
339 (Álvarez & Aldaya, 1985) as well as chloritoid (Booth-Rea *et al.*, 2004). The strike of the foliation
340 on the western flank of Sierra Almagrera (the studied area) oscillates between N045E and N100E,
341 with an average dip of around 25-30°SE-S that can reach up to 45°SE-S at El Arteal mine (Figure 1-
342 b). Although stretching lineation is not always observed, deformed quartz veins (V-Qtz1) indicate a
343 top to the West shearing (Figure 2-a).

344 The Raman study of graphitic carbon yields R2 ratios from 0.12 to 0.21 (mode: 0.18; n=8, in
345 3 samples), corresponding to temperatures ranging between 545 and 590 °C. These results are in
346 agreement with the temperatures of 535-550 °C determined using the same method in the Calar
347 Alto unit from the Sierra de Los Filabres (Augier *et al.*, 2005b). Phengite shows Si contents ranging
348 from 3.31 to 3.05 a.p.f.u (n=4, in 2 samples), corresponding to an estimated pressure ranging from
349 2.2 kbar at 545 °C to 9.7 kbar at 590 °C (Massonne & Schreyer, 1987). These pressures are similar
350 to those obtained in the Calar-Alto unit in the Sierra de Los Filabres (10±0.7 kbar to 3.1±0.3 kbar)
351 (Augier *et al.*, 2005b).

352 4.2. Vein and fluid inclusion petrography

353 According to their geometry, petrography and position relative to the host rock foliation, five
354 types of veins can be defined (Table 2). Table 3 summarizes the characteristics of the fluid
355 inclusions observed within each vein.

356 4.2.1 V-Qtz1, quartz veins parallel to host-rock foliation

357 V-Qtz1 veins (thickness less than 30 cm) may be found in both structural blocks (Figure 2-a).
358 These quartz veins are characterised by high-temperature recrystallization mechanisms with
359 granoblastic euhedral texture, with grains of about 200 µm showing triple points with an angle of

1
2 360 120° (Figure 2-b) or lobate grain boundaries interpreted as due to grain boundary migration (Jessell,
3
4 361 1987, Passchier & Trouw, 2005, Stipp & Kunze, 2008) (Figure 2-c). No primary inclusions are
5
6 362 observed in Qtz1 grains, and transgranular fluid inclusion planes are only observed in the Sierra
7
8 363 Almagrera mining district. Relative chronology criteria indicate that Qtz1-tg1 predates Qtz1-tg2.
9
10 364 Each set of plane displays a distinct orientation (Figure 2-d-e-f; Table 3).

13 365 **4.2.2 V-Qtz2, quartz veins parallel to or oblique to host-rock foliation**

16 366 V-Qtz2 (thickness of about 10 cm) are oblique to the rock foliation along certain sections of
17
18 367 the vein, while other parts are parallel (Figure 3-a). Since V-Qtz2 partly crosscuts the rock foliation,
19
20 368 they are considered as postdating V-Qtz1, which is parallel to the foliation. V-Qtz2 are
21
22 369 characterized by anhedral quartz grains of about 3-5 mm, showing undulose extinction. These
23
24 370 grains are characterized by wave-shaped grain-boundaries and subgrain boundaries. Subgrain
25
26 371 rotation and bulging recrystallization processes can be distinguished (Figure 3-b). Microstructures
27
28 372 indicate dynamic recrystallization processes at slightly lower temperatures than V-Qtz1 (Figure 3-b;
29
30 373 Passchier & Trouw, (2005)). Fluid inclusions in V-Qtz2 are found within intragranular (Qtz2-ig)
31
32 374 (Figure 3-b-c) or transgranular planes (Qtz2-tg) (Figure 4-a-b-e). The direction and dip of Qtz2-ig
33
34 375 fluid inclusion planes are randomly distributed (Figure 3-e) throughout the vein, but are parallel to
35
36 376 each other within a single grain. This suggests that these veins are related to crystallographic
37
38 377 directions reactivated during crystal plastic deformation rather than tectonic fracturing. Qtz2-tg
39
40 378 veins are parallel to each other and to the walls of V-Qtz2 (Figure 4-b-e). They were likely
41
42 379 produced by crack-and-seal deformation.

47 380 **4.2.3 V-Qtz3, oblique veins from the mining district**

50 381 V-Qtz3 are composed of euhedral quartz associated with hematite, developed in veins
51
52 382 (thickness < 5 cm) oblique to the host-rock foliation or in voids. Although euhedral Qtz3 overgrows
53
54 383 Qtz2 (Figure 4-b), it is never intersected by Qtz2-tg. Isolated primary fluid inclusions are
55
56 384 interpreted as contemporaneous to crystal growth (Qtz3-p; Figure 4-f). Hematite is found within
57
58 385 microfissures extending from the wall rock to Qtz2 (Figure 4-b-d) and in voids between euhedral
59
60

1
2 386 Qtz3 (Figure 4-a-b). The lack of microfractures affecting Qtz3 and the almost systematic
3
4 387 association of Qtz3 with hematite minerals suggest that both minerals grew during the same
5
6 388 mineralization event.
7

8 9 389 **4.2.4 V-ore, oblique mineralised veins from the mining district**

10
11 390 An extensive study of ore mineralogy in the mining district (Morales Ruano, 1994) shows the
12
13 391 occurrence of abundant siderite, barite, pyrite, marcasite, galena, chalcopryrite, sphalerite,
14
15 392 tetrahedrite-tennantite, veenite, gersdorffite and bournonite and trace amounts of pyrrhothite,
16
17 393 bismuthinite, arsenopyrite and bravoite. Our sampled veins (V-ore) show only part of this
18
19 394 paragenesis.
20

21
22 395 V-ore veins crosscut V-Qtz1 (Figure 5-a), V-Qtz2 and V-Qtz3 (Figure 4-a). The thickness of
23
24 396 the sampled V-ore veins can reach several dm. They are distributed in two main clusters striking
25
26 397 N000-160E and N120-130E. Micro-euhedral quartz (0.5-1.0 mm) is observed on the walls of V-ore
27
28 398 (Figure 5-a) predating siderite formation. Pyrite is included in siderite (Figure 5-c). Galena occurs at
29
30 399 the contact between siderite and barite (Figure 5-b). The mineral sequence can be summarized as
31
32 400 follows: micro-euhedral quartz-siderite-pyrite-galena-barite (Figure 5-c).
33

34
35 401 Qtz-ore-tg inclusions are parallel to the wall rock and crosscut several micro-euhedral quartz
36
37 402 grains. Fluid inclusions in siderite and barite are observed along cleavage planes and interpreted as
38
39 403 primary (Figure 5-d-e).
40

41 42 43 404 **4.2.5 V-Cal, oblique calcite veins from the subsident area**

44
45 405 These lenticular tension gashes crosscut V-Qtz2 and attain a length of several cm with an
46
47 406 opening of a few mm (Figure 6-a). Fluid inclusions are found as clusters and are interpreted as
48
49 407 primary (Figure 6-b-c).
50

51 52 53 408 **4.3. Microthermometry and Raman results**

54
55 409 Table 3 presents data concerning the size, shape and filling of the fluid inclusions. The
56
57 410 characteristic phase-transition temperatures and calculated compositions of fluid inclusions are
58
59
60

1
2 411 reported in Table 4 and Figure 7. Aqueous carbonic fluid inclusions are recorded in quartz veins
3
4 412 (Qtz1-tg1, tg2, Qtz2-ig, Qtz2-tg and Qtz3-tg), whereas aqueous fluid inclusions are recorded in ore
5
6 413 veins.

9 414 **4.3.1 Fluid inclusions in Qtz1**

10
11 415 The salinity of Qtz1-tg1 ranges between 9.7 and 22.6 mass% NaCl_{eq.}, with T_h (L) between
12
13 416 319 and 350 °C. The volatile phase is predominantly CO₂ (70-85 vol%), with minor amounts of
14
15 417 CH₄ (10-17 vol %) and N₂ (0-18 vol%).

16
17
18 418 The salinity of Qtz1-tg2 ranges between 21.6 and 23.8 mass% NaCl_{eq.}, with T_h (L) between
19
20 419 305 and 344 °C. The volatile phase is predominantly CO₂ (89-97 vol %), with minor amounts of
21
22 420 CH₄ (0-8 vol%) and N₂ (0-7 vol%).

23 421 **4.3.2 Fluid inclusions in Qtz2**

24
25
26
27
28 422 The salinity of Qtz2-ig ranges between 11.9 and 20.6 mass% NaCl_{eq.}, with T_h (L) between 220
29
30 423 and 400 °C. This broad scatter of homogenization temperatures is attributed to volume modification
31
32 424 of fluid inclusions during high-temperature deformation (Vityk *et al.*, 1995, Bodnar, 2003,
33
34 425 Diamond *et al.*, 2010). Therefore, we only consider T_h of intact inclusions with the smallest gas
35
36 426 bubbles (flw > 65 vol %), resulting in a range from 220 to 355 °C. The volatile phase is dominated
37
38 427 by CO₂ (87-98 vol %), with minor amounts of CH₄ (1-8 vol %) and N₂ (1-7 vol %).

39
40
41 428 The salinity of Qtz2-tg ranges between 0.1 and 2.4 mass% NaCl_{eq.}, with T_h (L) between 290
42
43 429 and 330 °C. Raman spectroscopy shows that the volatile phase is predominantly CO₂ (57-85 vol %),
44
45 430 with presence of CH₄ (5-30 vol %), N₂ (7-12 vol %) and H₂S (1-5 vol %).

46 431 **4.3.3 Fluid inclusions in Qtz3**

47
48
49
50
51 432 The salinity of Qtz3-p ranges between 12.7 and 20.9 mass% NaCl_{eq.}, with T_h (L) between 235
52
53 433 and 310 °C. The volatile phase is predominantly CO₂ (91-99 vol %), with minor amounts of CH₄ (1-
54
55 434 7 vol %) and N₂ (0-5 vol %).

56
57
58 435

4.3.4 *Fluid inclusions in Qtz, Sd and Brt from V-ore veins*

The salinity of Qtz-ore-tg ranges between 18.4 and 25.0 mass% NaCl_{eq.}. Methane (traces) is the only volatile present. $T_h(L)$ ranges between 150 and 248 °C.

The salinity of Sd-p ranges between 15.4 and 24.6 mass% NaCl_{eq.}. Because no hydrohalite melting or clathrate dissociation temperature could be observed, our calculation is based on the final ice melting only and does not take into account the complexity of the fluid system. Therefore, some data yield salinity higher than halite saturation in the H₂O-NaCl system. $T_h(L)$ is observed between 110 and 222 °C. Such a large variation is likely related to leakage within this highly cleavable mineral (Bodnar, 2003). Raman spectroscopy shows that CH₄ is the only volatile in the gas phase.

The salinity of Brt-p ranges between 20.7 and 25.8 mass% NaCl_{eq.}. Again, because hydrohalite is never observed, our calculations only take account of $T_m(ice)$ and the complexity of the system is not fully expressed. Therefore, some of our data show salinities higher than NaCl saturation in the H₂O-NaCl system. $T_h(L)$ is observed between 237 and 335 °C. Although the inclusions were carefully checked before and after measurements, leakage before microthermometric experiments cannot be excluded (Ulrich & Bodnar, 1988, Bodnar, 2003), so these values in barite should be considered very carefully. Raman spectroscopy shows that the volatile phase is predominantly composed of CO₂ (45-93 vol %) (although present in small amount) and N₂ (5-52 vol %) with minor CH₄ (0-5 vol %).

4.3.5 *Fluid inclusions in calcite from V-Cal*

The salinity of Cal-p ranges between 11.8 and 18.4 mass% NaCl_{eq.}, with $T_h(L)$ between 67 and 87 °C (Figure 7). Raman spectroscopy does not allow us to identify the nature of the gas phase.

4.4. Halogen chemistry

For V-Qtz1, a Cl/Br molar ratio of 1000 is obtained by crush-leach analysis and LA-ICPMS for a chlorinity of 4200 mmol/kg solution (Figure 8). The crushing experiments release fluids derived from Qtz1-tg1 and Qtz1-tg2 as well as the fluid contained at grain boundaries.

1 461 Sd-p and Brt-p yield a Cl/Br ratio of between 3 500 and 10 000 for a chlorinity between 4 200
2
3
4 462 and 5 400 mmol/kg solution, respectively. The Cl/Br ratio of Brt-p obtained with LA-ICP-MS is
5
6 463 between 1 200 and 4 500 (Figure 8). The other populations of fluid did not give an interpretable
7
8 464 signal.
9

10 465 **4.5. Major and trace element chemistry**

11
12
13
14 466 In both types of fluids (Qtz1-tg1 (n=8), Qtz2-tg (n=2), Qtz3-p (n=4) and Brt-p (n=9))
15
16 467 inclusions major (Na, K, Mg) and trace elements (Li, Mn, Fe, Cu, Zn, Sr and Ba) have been
17
18 468 measured (Table 5, Figure 9). The other generations of fluids do not give any interpretable signals.
19

20
21 469 In Qtz1-tg1 high salinity fluid, Na content ranges from 27000 to 122 000 ppm, K from 2000
22
23 470 to 7600 ppm, yielding Na/K ratio ranging from 10 to 30. Mg content is relatively variable (100-
24
25 471 1600ppm). Li content is relatively high (200 to 1000 ppm). Mn, Fe, Ba and Sr display noticeable
26
27 472 concentration (Table 5, Figure 9).
28

29 473 On the contrary, Qtz2-tg having very low salinity show lower cation content and Na/K ratio is
30
31 474 ranging from 1 to 6. Due to the low salinity fluid, few data could be obtained.
32

33
34 475 Qtz3-p fluids displayed similar values as for Qtz1-tg1 (Na around 70 000 ppm). However K
35
36 476 content is lower (1500 ppm) and consequently Na/K ratio is higher (around 50). Mg, Sr, and Mn
37
38 477 content are the highest (Table 5, Figure 9).
39

40 478 In Brt-p fluids, Ba and Sr content could not be measured due to matrix contamination. Na
41
42 479 content is slightly lower than those of Qtz1-tg1 (20000 and 65000 ppm) whereas K content is
43
44 480 ranging from 2600 and 9500 ppm (Na/K: 4 to 10). It can be notice that Zn content could reach 4700
45
46 481 ppm. However, we cannot exclude a contribution of the barite crystal (Table 5, Figure 9).
47
48

49 482 **4.6. Stable isotopes**

50
51
52 483 $\delta^{13}\text{C}$ in siderite ranges between -9.5 and -10.9 ‰_{V-PDB} (n=4), while $\delta^{18}\text{O}$ ranges between
53
54 484 20.6 and 22.5 ‰_{V-SMOW} (Table 6). $\delta^{18}\text{O}$ in barite ranges from 13.0 to 13.2 ‰_{V-SMOW} (n=2), and
55
56 485 $\delta^{34}\text{S}$ (n=4) from 19.4 to 23.1 ‰_{V-CDT}. Pyrite (n=3) yields $\delta^{34}\text{S}$ between 5.4 and 6.4 ‰_{V-CDT} and
57
58 486 galena (n=3) yields $\delta^{34}\text{S}$ between -2.4 and 8.3 ‰_{V-CDT}.
59
60

1
2 487 Table 6 reports the $\delta^{18}\text{O}$ values of minerals containing fluid inclusions. White micas from the
3
4 488 host-rock yield δD values of -52 ± 1 ‰ V-SMOW . $\delta\text{D}_{\text{fluid}}$ values from Qtz1 sampled in the subsident
5
6 489 area (recrystallised quartz devoid of visible inclusions) range between -33 and -36 ‰ V-SMOW .
7
8 490 Former trapped fluid inclusions appear to have been transported to the grain boundaries during
9
10 491 hydrolytic weakening (e.g. (Kerrick, 1976, Wilkins & Barkas, 1978, Johnson & Hollister, 1995,
11
12 492 Hollister, 1990, Bakker & Jansen, 1990, 1994), so it is likely that remnants of this fluid were
13
14 493 measured. In the mining district, V-Qtz1 veins host Qtz1-tg1 and Qtz1-tg2 type inclusions. The
15
16 494 transgranular fluid inclusion planes show δD values between -28 and -32 ‰ V-SMOW , possibly
17
18 495 reflecting the influence of δD inherited from earlier fluids displaced to grain boundaries during
19
20 496 quartz recrystallization.
21

22
23
24 497 $\delta\text{D}_{\text{fluid}}$ from Qtz2-ig and Qtz3-p inclusions cover a similar range between -23 and -36 ‰ V-SMOW
25
26 498 (Table 6, Figure 10). $\delta\text{D}_{\text{fluid}}$ from Qtz2-tg (selected section with dominant Qtz2-tg inclusions
27
28 499 in the quartz grains) display a larger range of values between -17 and -48 ‰ V-SMOW (Table 6,
29
30 500 Figure 10).
31

32
33 501 V-ore veins are significantly more D-depleted. $\delta\text{D}_{\text{fluid}}$ of Sd-p range between -65 and -80 ‰
34
35 502 V-SMOW . $\delta\text{D}_{\text{fluid}}$ of Brt-p ranges between -53 and -69 ‰ V-SMOW (Table 6, Figure 10).
36

37 503 **5. Discussion**

38 504 **5.1. Key criteria to reconstruct the fluid sequence**

39
40
41 505 *Early fluid stage:* Ductile deformation affecting V-Qtz1 and V-Qtz2 in the Sierra Almagrera
42
43 506 is compatible with top-to-the-W / top-to-the-SW extensional shearing similar to that observed in the
44
45 507 Sierra de los Filabres (Augier *et al.*, 2005c) (Figure 1). This deformation is not dated in the Sierra
46
47 508 Almagrera. The only known age constraint is given by the youngest ductile extensional stages
48
49 509 recognized within the Betics metamorphic pile, which are dated around the Langhian-Serravalian
50
51 510 boundary at 14 Ma (Gomez-Pugnaire *et al.*, 2004, Platt *et al.*, 2006, Gomez-Pugnaire *et al.*, 2012).
52

53
54
55 511 Although no fluid inclusions are observed in V-Qtz1 veins sampled from the subsident area,
56
57 512 crushing techniques allowed us to extract a fluid, which could then be analysed for its δD . This
58
59
60

1
2 513 suggests that fluid inclusions trapped prior to plastic deformation are displaced towards grain
3
4 514 boundaries during recrystallization processes (Kerrick, 1976, Wilkins & Barkas, 1978, Johnson &
5
6 515 Hollister, 1995) and are then partly preserved. The calculated equilibrium temperature between this
7
8 516 fluid and host-rock, based on hydrogen isotope fractionation, is comprised between 488 and 520 °C
9
10 517 (Table 6), which is in agreement with ductile conditions. Plastically deformed or dismembered
11
12 518 inclusions are found within intragranular planes of V-Qtz2 (Qtz2-ig), while non-deformed
13
14 519 inclusions are found within transgranular planes affecting V-Qtz1 in the mining district where V-
15
16 520 ore barite veins are also frequently present. Transgranular planes result from the healing of former
17
18 521 open cracks (Lespinasse, 1999, Lespinasse et al., 2005), and thus more brittle conditions are
19
20 522 required than for intragranular planes. As a consequence, Qtz2-ig likely formed at conditions more
21
22 523 ductile than Qtz1-tg1, 2.

24
25
26 524 Similar microthermometric phase transitions are observed for Qtz2-ig and Qtz1-tg1, 2
27
28 525 (average T_h around 340 °C and with comparable maximum salinity). Relative chronology criteria
29
30 526 indicate that Qtz1-tg1 predates Qtz1-tg2, but no other direct data allow us to constrain the
31
32 527 chronological position of Qtz1-tg (1, 2) in the general fluid history. Two interpretations can be
33
34 528 proposed. The dominant NW-SE strike of Qtz1-tg1 may be consistent with late Tortonian
35
36 529 shortening directions associated with strike-slip tectonics (Montenat & Ott D'estevou, 1990). This
37
38 530 deformation occurred prior to the Messinian N-S to NNE-SSW shortening that could correspond to
39
40 531 the subsequent Qtz1-tg2 fluid inclusion planes. In such a scenario, the transgranular fluid inclusions
41
42 532 could be coeval with V-ore mineralizing events displaying similar tectonic directions, and thus
43
44 533 would not correspond to an early fluid trapped during the brittle-ductile transition.

45
46
47
48 534 An alternative explanation would be that both kinds of microcracks are related to brittle
49
50 535 extensional fracturing, implying that the tectonic regime previously expressed by ductile
51
52 536 deformation belongs to an earlier stage of exhumation. In such a case, the brittle deformation would
53
54 537 predate the onset of a Late Miocene transcurrent regime related to the mineralizing events.
55
56 538 Therefore, σ_3 measured normal to the microcracks would be similar for both the extensional and
57
58
59
60

1
2 539 transcurrent regimes, with the result that this question cannot be resolved solely on the basis of
3
4 540 structural criteria. If fluids were trapped soon after the ductile-brittle transition for quartz, this
5
6 541 would explain certain similarities of the microthermometry and salinity data with Qtz2-ig fluid
7
8 542 inclusions trapped during this transition.
9

10 543 Intermediate fluid stage: Qtz2-tg fluids are characterised by a much lower salinity than
11
12 544 observed in the other types of fluid inclusions. Since Qtz2-tg never affects V-Qtz3 nor V-Cal, this
13
14 545 suggests an episodic arrival of low-salinity fluid after the formation of V-Qtz2 but prior to V-Qtz3
15
16 546 and V-Cal. Considering the youngest ages inferred for ductile deformation in the eastern Betics
17
18 547 (around the Langhian-Serravalian boundary), the exhumation of this part of the Sierra Almagrera
19
20 548 within the brittle domain probably occurred during Langhian to Serravalian times. Only marine
21
22 549 sediments of Serravalian age are preserved further north in the Aguilas block (Griveaud *et al.*,
23
24 550 1990). Younger sediments of Late Serravalian – Early Tortonian age recognized further west in the
25
26 551 Huerca Overa Basin (Pedrera *et al.*, 2010) are represented by alluvial fan deposits reflecting the
27
28 552 uplift of mountain ranges prior to the return of marine conditions in the Vera Basin from Late
29
30 553 Tortonian times onwards (Figure 1). The uplift of the Sierra de los Filabres bordering the Huerca
31
32 554 Overa Basin has been linked to a local N-S extension (Augier *et al.*, 2005a) or the onset of
33
34 555 transcurrent tectonics (Montenat & Ott D'estevou, 1990). Regardless of the associated tectonic
35
36 556 regime at this time, the paleogeography suggests that hydrogeological conditions within the brittle
37
38 557 crust favoured the input of meteoric water from the uplifted ranges into the upper reservoir, but
39
40 558 prior to the Late Tortonian return to marine conditions.
41
42
43
44

45 559 Pre-ore fluid stage: The obliquity with respect to the host-rock foliation and the lack of
46
47 560 undulose extinction in the euhedral quartz shows that V-Qtz3 formed within the brittle domain.
48
49 561 Euhedral Qtz3 formed during the same event that led to the formation of hematite. The input of Fe
50
51 562 in the fluid is related here to an increase of salinity. Although oxidizing conditions prevailed at a
52
53 563 certain stage of the fluid evolution, it is possible that early siderite was subsequently oxidized.
54
55
56
57
58
59
60

1
2 564 Ore fluid stage: V-ore veins crosscut V-Qtz3 (Figure 4-a). The maximum salinities are
3
4 565 observed either in fluid inclusions from transgranular planes within early micro-euhedral quartz on
5
6 566 the wall-rock (Qtz-ore-tg), or in primary fluid inclusions from siderite and barite (Sd-p and Brt-p).
7
8 567 The formation of siderite postdating V-Qtz3-hematite veins not only indicates the ongoing input of
9
10 568 Fe in the fluid, but also a shift towards reducing conditions. Quartz and siderite trapped fluids at
11
12 569 lower temperatures (T_h of Sd-p around 190 °C) compared with the pre-ore fluid stage (T_h of Qtz3-p
13
14 570 around 265 °C). V-ore vein sets have two main strike directions: N000E-N340E and N120E-
15
16 571 N130E. The N-S trend is coherent with the Messinian direction of horizontal shortening and E-W
17
18 572 extension, being related to the major transcurrent activity of the Palomares Fault Zone. The
19
20 573 interpretation of fluid inclusions in barite is more problematic. The data appears to indicate an
21
22 574 increase of T_h compared to the estimated conditions of siderite formation (Figure 7), but T_h
23
24 575 obtained from this kind of mineral are usually considered to be overestimated (Ulrich & Bodnar,
25
26 576 1988). This raises the question of the chronological position of N-S to NNE-SSW-striking fluid
27
28 577 inclusion planes belonging to Qtz1-tg2, since both Brt-p and Qtz1-tg2 show closely similar T_h
29
30 578 values and high salinities (Figure 7). It is possible that this similarity is just a coincidence or maybe
31
32 579 Qtz1-tg2 inclusions in quartz reflect a thermal pulse that leads to values typical of Brt-p.
33
34
35
36

37 580 Late fluid stage: Inclusions in calcite record lower T_h around 80 °C, suggesting formation at a
38
39 581 more superficial position. The relative chronology of this late stage in the fluid sequence could be
40
41 582 debated since the calcite veins were not sampled in the same structural block as V-ore veins. The
42
43 583 only chronological criterion is the crosscutting geometry with V-Qtz2.
44
45
46

47 584 **5.2. P-V-T-X evolution**

48
49 585 The Raman spectrometry study of graphitic schists constrains the maximum temperature
50
51 586 attained by the host-rock to 545-587 °C. These results are in agreement with metamorphic peak
52
53 587 temperatures of the Nevado-Filábride complex obtained in other parts of the orogen (De Jong, 2003,
54
55 588 Augier *et al.*, 2005b).
56
57
58
59
60

1
2 589 The P - T ranges of fluid inclusion entrapment are constrained by the isochores and geothermal
3
4 590 gradients (Figure 11). For the Sierra Almagrera, geothermal gradient data are poorly documented.
5
6 591 The only available data comes from the Sierra Nevada located to the West of Sierra Almagrera,
7
8 592 where a gradient of 60 °C/km under lithostatic conditions is indicated for the final stages during
9
10 593 ductile deformation (Gomez-Pugnaire & Fernandez-Soler, 1987, Bakker *et al.*, 1989, Jabaloy *et al.*,
11
12 594 1993, Augier *et al.*, 2005b). A gradient of 30 °C/km is arbitrarily taken as an upper limit,
13
14 595 corresponding to the European average anorogenic gradient.

15
16
17 596 In the absence of other metamorphic constraints, hydrogen isotopes can be used to assess the
18
19 597 temperature of equilibrium between fluid inclusions and mica-rich host-rock (Tarantola *et al.*,
20
21 598 2007). In the case of isotopic equilibrium, P - T boxes are also constrained by the minimum and
22
23 599 maximum values of hydrogen equilibrium temperatures (Table 6 and Figure 11).

24
25
26 600 Early fluid stage: Qtz2-ig inclusion shapes range from euhedral to dismembered (Tarantola *et*
27
28 601 *al.*, 2010 and 2012), with large variations of the gas filling ratio. This is indicative of plastic
29
30 602 deformation and would thus be related to lithostatic pressure conditions. The box shown in Figure
31
32 603 11 is also constrained by minimum and maximum hydrogen equilibrium temperatures since the
33
34 604 calculated temperatures are of the order of 400-520 °C (Table 6).

35
36
37 605 Transgranular fluid inclusion planes Qtz1-tg1 and Qtz1-tg2 indicate brittle behaviour within
38
39 606 the quartz vein, but the mica-rich host-rock may still have been affected by ductile deformation.
40
41 607 Fluids may have been trapped during the brittle-ductile transition of mica-rich lithologies within a
42
43 608 temperature and pressure range already corresponding to brittle rheology for the quartz. In such a
44
45 609 case, both Qtz1-tg1 and Qtz1-tg2 possibly formed under a lithostatic regime. As an alternative
46
47 610 hypothesis, these microcracks may be indicative of a hydrostatic regime due to late Miocene
48
49 611 transcurrent tectonics that formed V-ore veins in the brittle domain. In fact, Qtz1-tg1/Qtz1-tg2
50
51 612 fluids seem to be in equilibrium with the host-rock (Table 6), but in strong disequilibrium with
52
53 613 respect to V-ore veins. In addition, the gas contents of Qtz1-tg1 and Qtz1-tg2 are more closely
54
55 614 similar than those of Sd-p and Brt-p fluid inclusions (Table 4). All these data suggest a resident

1
2 615 fluid derived from the lower reservoir rather than the presence of fluids of external origin in the
3
4 616 upper reservoir. Finally, this explains why Qtz1-tg1 and Qtz1-tg2 could be related to the early fluid
5
6 617 stage in the selected scenario (Figure 11). Thus, the rather large T and P range reflects the trapping
7
8 618 conditions of inclusions related to this stage between Qtz2-ig (400-520 °C and 270-380 MPa) and
9
10 619 Qtz1-tg1, 2 (440-480 °C and 110-230 MPa) (Figure 11).

12
13 620 Intermediate fluid stage: There is no evidence of whether transgranular Qtz2-tg planes formed
14
15 621 under a lithostatic or a hydrostatic fluid regime. From this intermediate stage of fluid evolution until
16
17 622 the final stages of fluid trapping, the hydrogen isotope fractionation seems to be no longer in
18
19 623 equilibrium between the fluid inclusions and the mica-rich host-rock (Table 6). Hydrogen
20
21 624 equilibrium temperature constraints do not allow us to define the P - V - T - X boxes. The decrease of
22
23 625 salinity related to an input of surficial fluids rather suggests an opening of the system under
24
25 626 hydrostatic conditions. The trapping conditions for these fluid inclusions are in the range 300-450
26
27 627 °C and 40-140 MPa (Figure 11).

28
29
30 628 Pre-ore fluid stage: Since the euhedral quartz Qtz3 veins were no longer affected by ductile
31
32 629 deformation and recrystallization processes, it is considered that they crystallized in the brittle
33
34 630 domain under hydrostatic pressure, within the P - T range: 250-380 °C and 40-120 MPa (Figure 11).

35
36
37 631 Ore fluid stage: Crystallization of quartz, siderite and barite occurred in an open system.
38
39 632 Hydrostatic conditions allow us to constrain the P - T range of entrapment for fluid inclusions at 160-
40
41 633 300 °C and 30-90 MPa in Qtz-ore-tg and at 120-260 °C and 20-80 MPa in Sd-p (Figure 11).
42
43 634 Unfortunately, the confidence on microthermometric data obtained on barite is low (Ulrich &
44
45 635 Bodnar, 1988). The observed homogenization temperatures would imply a significant increase of
46
47 636 the trapping temperature to 280-440 °C at 40-130 MPa. This could be explained by a magmatic
48
49 637 input from contemporaneous active volcanism, but it could also be related to an overestimation due
50
51 638 to stretched inclusions in barite. T_h and salinity of Brt-p are similar to Qtz1-tg2 inclusions, while
52
53 639 strike directions of barite V-ore veins are more or less parallel to Qtz1-tg2 fluid inclusion planes.
54
55 640 These inclusions in quartz support the hypothesis of a thermal pulse defined by inclusions in barite.
56
57
58
59
60

1
2 641 In fact, P - V - T - X data from Qtz1-tg2 (Figure 11) seem to indicate a significant increase of pressure
3
4 642 compared to Sd-p fluid trapping conditions, which is apparently incompatible with an ongoing
5
6 643 exhumation of the Sierra Almagrera. Hydrogen isotopic fractionation indicates a strong
7
8 644 disequilibrium between primary fluid inclusions from V-ore veins and the host-rock. On the
9
10 645 contrary, hydrogen isotope data for Qtz1-tg2 indicate a fluid in equilibrium, rather suggesting its
11
12 646 formation during an early fluid stage. This interpretation does not support the existence of a thermal
13
14 647 pulse.

15
16
17 648 Late fluid stage: The calcite stage is characterized by lower homogenization temperatures,
18
19 649 suggesting a cooling of the system down to 70-110 °C at 10-30 MPa hydrostatic pressure (Figure
20
21 650 11).

22 651 **5.3. Source of fluids**

23
24
25
26
27 652 Early fluid stage: Hydrogen isotope fractionation data showing equilibrium between fluid
28
29 653 inclusions and mica-rich host-rock suggest a resident fluid in the lower reservoir. The δD_{fluid} values
30
31 654 obtained from Qtz1 (early fluids displaced towards grain boundaries during recrystallization
32
33 655 processes) and Qtz2-ig ranging between -23 and -36 ‰ V -SMOW (Table 6, Figure 10) are compatible
34
35 656 with a fluid of metamorphic origin.

36
37
38 657 V-Qtz1 quartz grains also containing Qtz1-tg1 and Qtz1-tg2 fluids yield similar δD values ($-$
39
40 658 28 to -30 ‰ V -SMOW). Their halogen signatures plot along the seawater evaporation trend in
41
42 659 agreement with halite evaporation (Figure 8). At first sight, this would indicate a primary brine.
43
44 660 Two brine sources can be considered according to the geological history: Triassic and Messinian. It
45
46 661 is very unlikely that primary brines could have been preserved since Triassic times, considering the
47
48 662 metamorphic processes affecting the rocks in the lower reservoir. The other hypothesis would be to
49
50 663 explain Qtz1-tg1 and Qtz1-tg2 signatures as representing surficial brines coming from Messinian
51
52 664 pre-crisis evaporitic basins. This interpretation revives the hypothesis linking Qtz1-tg2 and Brt-p
53
54 665 inclusions during mineralization events. However, stable isotope results and P - V - T - X data rather
55
56 666 identify fluids trapped in Qtz1-tg1 and Qtz1-tg2 microcracks as resident fluids that have undergone
57
58
59
60

1
2 667 long-time fluid-rock exchange with the mica-rich host-rock. The interaction of fluids with black
3
4 668 graphite schists may have led to a Br enrichment (Yardley, 2005) of secondary brines derived from
5
6 669 the dissolution of Triassic evaporites, which could explain the position of the data points on the
7
8 670 seawater evaporation curve (Figure 8).

9
10 671 The variability observed in the salinity of both Qtz2-ig and Qtz1-tg1/Qtz1-tg2 fluids might
11
12 672 either reflect i) an original heterogeneity related to discontinuous interaction with Permo-Triassic
13
14 673 evaporites, ii) the effect of plastic deformation for Qtz2-ig (Diamond *et al.*, 2010), or iii) a mixing
15
16 674 between deep high-salinity and a low-salinity fluid end-members.

17
18
19 675 Intermediate fluid stage: Fluid isotope values obtained on Qtz2 grains containing Qtz2-tg also
20
21 676 incorporate the signature of fluids from the early stage displaced to grain boundaries during
22
23 677 recrystallization processes. δD_{fluid} values ranging from -17 to -48 ‰ $v_{\text{-SMOW}}$ are generally lower
24
25 678 than values obtained for the early fluid stage. δD values of the dilute fluid are thus D-depleted
26
27 679 compared to those of the early stage, with values that are unlikely to be buffered by the host-rock
28
29 680 (Table 6). This suggests the input of an external low-salinity fluid from the upper reservoir, which
30
31 681 did not interact with evaporites/metaevaporites (i.e. Permo-Triassic).

32
33
34
35 682 It is possible that the volume of low-salinity fluids was sufficient to dilute high-salinity fluids
36
37 683 from the early stage, or more likely, the lower ductile and the upper brittle reservoirs were not
38
39 684 connected during exhumation and thus behaved independently. The penetration of low-salinity
40
41 685 fluids is likely associated with the uplift of mountain ranges during the Serravalian and Early
42
43 686 Tortonian (Martínez-Martínez & Azañón, 2002, Platt, 2007) (Figure 12). However, in the absence
44
45 687 of $\delta^{18}\text{O}$ values and interpretable LA-ICP-MS data, it cannot be concluded whether this fluid is of
46
47 688 meteoric or basinal origin.

48
49
50 689 Pre-ore fluid stage: Hydrogen isotopic composition is not buffered by the host-rock (Table 6).
51
52 690 The enrichment of iron in the fluid led also to the formation of hematite in the voids between Qtz3
53
54 691 crystals (Figure 4-b and Figure 12). This stage corresponds to tectonic conditions in the brittle
55
56 692 domain.

1
2 693 The salinity is comparable to that in the early fluid stage. $\delta^{18}\text{O}_{\text{quartz}}$ is lower than for the early
3
4 694 fluid stage, and trapping temperatures define a $\delta\text{D}/\delta^{18}\text{O}_{\text{fluid}}$ signature shifted towards
5
6 695 basinal/meteoric water compositions. The major and trace elements (Na/K ratio around 50, Sr/Ba
7
8 696 ratio around 20 and Sr, Mg content, Table 5) of this fluid reflect a basinal origin (Yardley, 2005).
9
10 697 These data are coherent with mixing between low-salinity basinal/meteoric fluids and with an
11
12 698 upward migration of high-salinity fluids coming from the lower reservoir. This may reflect the
13
14 699 onset of transcurrent tectonics during this period, and a structural connection between the two
15
16 700 reservoirs through the brittle ductile transition zone (Figure 12).

17
18
19 701 Ore fluid stage: Although siderite from El Arteal in the mining district yields slightly lower
20
21 702 $\delta^{13}\text{C}$ (about 2 ‰, with values of -9.5 and -10.9 ‰_{V-PDB}) and slightly higher $\delta^{18}\text{O}$ (about 1 ‰_V
22
23 703 _{SMOW}), it can be compared with the siderite from Jaroso Ravine (Figure 1-b). The results from this
24
25 704 latter locality have been interpreted as indicative of meteoric water and low-temperature
26
27 705 hydrothermal conditions (Martinez-Frias *et al.*, 2007). However, $\delta^{13}\text{C}$ may also be buffered by the
28
29 706 metasedimentary sequence during fluid interaction, whatever the origin of the fluids.

30
31
32 707 The combination of δD and $\delta^{18}\text{O}$ values suggests a fluid with a magmatic or metamorphic
33
34 708 signature (Field & Fifarek, 1985). As well as having a high salinity, the fluids do not fit the
35
36 709 meteoric water line (Figure 10), thus contradicting the conclusions of Martinez-Frias *et al.* (2007).
37
38 710 Since $\delta\text{D}_{\text{fluid}}$ is strongly in disequilibrium with the host-rock, this implies an external source for the
39
40 711 ore fluid, so it cannot be of meteoric origin.

41
42
43 712 Fluids in siderite were trapped at lower temperatures than the previous fluid stages, and thus
44
45 713 at shallower depths (Figure 12). The fluid inclusions in siderite show higher values of salinity than
46
47 714 obtained for the earlier stages, reaching up to 25 mass% NaCl_{eq} . (Figure 7, Table 4). Cl/Br data
48
49 715 show that the fluid is Br-depleted and far from the seawater evaporation trend. As Br is not easily
50
51 716 incorporated in halite, dissolution of halite would yield this type of fluid. Cl/Br ratios thus indicate
52
53 717 signatures that could be compared to secondary brines (Banks *et al.*, 2000) resulting from
54
55 718 dissolution of evaporites (Figure 8).

1 719 The strong salinity increase might result from a combination of volcanism in the Palomares
2
3 720 Fault Zone, as suggested by δD and $\delta^{18}O$ values (Figure 10), and dissolution of evaporites as
4
5
6 721 suggested by their halogen signatures (Figure 8). The strike direction of the veins is coherent with
7
8 722 the Messinian strike-slip regime related to major activity of the Palomares Fault Zone (Montenat *et*
9
10 723 *al.*, 1987, Booth-Rea *et al.*, 2004). Of major interest here is the $\delta^{34}S$ composition of barite, which is
11
12 724 more closely comparable to Miocene sea water (Claypool *et al.*, 1980, Morales Ruano *et al.*, 1995)
13
14
15 725 than Triassic values. Therefore, the increase of salinity in the ore fluid stage compared to previous
16
17 726 stages could also be related to secondary brines linked to the dissolution of Messinian evaporites
18
19 727 rather than exclusively of Triassic evaporites. Dissolution of Messinian marginal evaporites
20
21 728 (deposited from 5.96 to 5.67 Ma ago in the Sorbas basin) (Clauzon *et al.*, 1996, Bourillot *et al.*,
22
23 729 2009) is a possible scenario (Figure 12). These Messinian evaporites preceded the main sea-level
24
25
26 730 drop related to the peak of the salinity crisis (5.60-5.46 Ma). Pre-incision Messinian evaporitic
27
28 731 deposits were available, as revealed by the “Formation à blocs” in the Vera basin, which reworked
29
30 732 Messinian early gypsum during the main incision event (Figure 12) (Clauzon, 1980, Clauzon *et al.*,
31
32 733 1996). Messinian sediments from Las Herrerias (Figure 1) were mineralised prior to the main
33
34 734 Messinian incision (Alvado, 1986, Fortuin *et al.*, 1995, Booth-Rea *et al.*, 2004), and such a scenario
35
36 735 would provide a relatively accurate dating of the mineralizing event around 5.65 Ma (Figure 12).
37
38

39 736 A thermal pulse at constant salinity is suspected because the fluid trapping conditions in barite
40
41 737 exceed 400 °C, but this result should rather be considered as an artefact arising from this particular
42
43 738 mineral (Figure 12). If the high-K calc-alkaline, shoshonitic and ultrapotassic magmatism were
44
45 739 related to mineralization during the ore-fluid stage, this could represent a possible metal source. The
46
47 740 high contents of K or metals such Zn or Cu in fluid inclusions (Table 5, Figure 9) tend to support
48
49 741 this hypothesis, but a leaching of basement rocks could also be an alternative explanation.
50
51

52 742 Late fluid stage: Homogenization temperatures of fluid inclusions within calcite around 80 °C
53
54 743 suggest deep burial or a shallow expression of hot fluids. The salinity of these fluids may be
55
56 744 compared to the salinity of early and pre-ore stages. Calcite veins may correspond to a shallow
57
58
59
60

1
2 745 expression of deeper fluid flows, recorded as veins currently cropping out in the uplifted block
3
4 746 represented by the mining district (Figure 12). In such a case, the superficial equivalent of rocks in
5
6 747 the central block may have been eroded during the subsequent uplift, but preserved in the subsident
7
8 748 block to the West. A second hypothesis is that these calcite veins only developed during a later
9
10 749 stage at lower temperature.

11
12
13 750 Fluids trapped as fluid inclusion planes during the early stage are characterized by a rather
14
15 751 low density of the CO₂-rich volatile phase. The significant presence of CH₄ (around 20% of the
16
17 752 volatile molar composition) is not strictly expected in the case of water-graphite equilibrium
18
19 753 (Dubessy, 1984, Huizenga, 2001, 2011). Such a distribution of volatiles is fairly common in
20
21 754 metamorphic environments at around 350-450 °C, where local equilibrium is reached between
22
23 755 water and graphite. Through mixing with other fluids, this contributes to the common metamorphic
24
25 756 signature found in most retrograde fluids during exhumation (Cathelineau *et al.*, 1993, Boiron *et al.*,
26
27 757 2003). At lower temperatures, in the presence of graphite, CH₄ is expected to be the dominant
28
29 758 species if redox conditions are moderately reducing. This applies in the case of a predominance of
30
31 759 CH₄ in fluid inclusions during the precipitation of siderite at the beginning of the Ore stage, which
32
33 760 occurred with a T_h around 190 °C. The precipitation of siderite from Fe²⁺-rich solutions requires a
34
35 761 significantly low fO_2 and an increase in fCO_2 .

36 37 38 39 40 762 **6. Conclusions**

41
42
43 763 Fluid circulation events are recorded within the studied veins at different positions of the
44
45 764 Sierra Almagrera metamorphic belt during its exhumation. The general P - T path is characterized by
46
47 765 an evolution from lithostatic to hydrostatic conditions. Despite the rather exceptional constant fluid
48
49 766 composition throughout exhumation, different geological contexts associated with fluid circulation
50
51 767 can be considered: i) a first stage during which the host-rock passed through the brittle-ductile
52
53 768 transition and the quartz trapped metamorphic fluids, ii) a second stage when the host-rock
54
55 769 definitively entered the brittle domain and predominantly collected shallower fluids from the upper
56
57
58 770 reservoir and, iii) a final stage, related to ore formation and possibly magmatism as well, resulting
59
60

1
2 771 in a marked tectonic change that modified the relative hydrogeologic independence between the
3
4 772 deeper and upper reservoirs.

5
6 773 More generally, the tectonic and paleotopographic evolution of the Sierra Almagrera leads us
7
8 774 to consider two stages in the fluid circulation history. Prior to the transcurrent tectonic regime, the
9
10 775 metamorphic rocks of the Sierra Almagrera were exhumed as a whole, and V-Qtz1 and V-Qtz2
11
12 776 veins were developed throughout the studied area. The onset of transcurrent tectonics had two
13
14 777 consequences: i) it localized the deformation and associated fluid pathways within the brittle crust
15
16 778 and, ii) it generated local transtension and transpression leading to final exhumation of the central
17
18 779 area corresponding to the mining district where V-Qtz3 and V-ore veins are found.

19
20
21 780 The first record of exhumation is characterized by ductile-brittle deformation related to
22
23 781 extensional tectonics. We propose that, during this early stage, metamorphic brines resulted from
24
25 782 the dissolution of Triassic evaporites. Low-salinity fluids were then recorded as the structural unit
26
27 783 progressively entered the brittle domain. These low-salinity fluids are likely related to the
28
29 784 penetration of basinal or meteoric waters from the surface, favoured by a hydraulic gradient related
30
31 785 to the uplift of mountain ranges during late Serravalian to early Tortonian times.

32
33
34 786 The upper fluids could have retained their specific characteristics until the present-day, but
35
36 787 the geodynamic changes related to the onset of Trans-Alboran tectono-volcanism modified the
37
38 788 hydrogeological decoupling between the lower and upper reservoirs. The pre-ore stage is
39
40 789 characterized by the occurrence of brittle quartz veins related to intermediate salinity and
41
42 790 homogenization temperatures indicative of mixing between meteoric or basinal fluids and the
43
44 791 upward migration of high-salinity fluids coming from the lower reservoir. These fluids are similar
45
46 792 to those from the early fluid stage. They have a volatile phase dominated by CO₂ but devoid of CH₄,
47
48 793 being associated with Fe which is expressed by the formation of hematite under oxidizing
49
50 794 conditions, but possibly after the crystallization of primary siderite. This pre-ore stage can be
51
52 795 interpreted as the first evidence of the influence of volcanism.

53
54
55
56
57
58
59
60

1
2 796 Reducing conditions prevailed at a later stage of Fe-rich fluid migration. This is reflected by
3
4 797 the formation of siderite and Fe sulphides in the mining district, and is related to the activity of the
5
6 798 Palomares sinistral fault zone during the Messinian. An evolution towards more oxidizing
7
8 799 conditions led to the formation of galena and barite, whose $\delta^{34}\text{S}$ signatures indicate the involvement
9
10 800 of Miocene sulphate. This suggests the involvement of a second type of secondary brines (Ore
11
12 801 stage) which may have dissolved Messinian evaporites from the Vera Basin. Since the marginal
13
14 802 evaporitic basins in the Betics are dated at around 5.96 to 5.67 Ma (Sorbas basin; Bourillot *et al.*
15
16 803 (2009)), and since the Las Herrerias stratabound ore-deposits were incised during the main
17
18 804 Messinian salinity crisis and sea-level fall in the Mediterranean domain (5.6-5.46 Ma), this scenario
19
20 805 would provide an accurate constraint on the age of the mineralization stage around 5.65 Ma
21
22

23
24 806 The overall evolution of fluid migration in this part of the Betic Cordillera points out the role
25
26 807 of three main driving forces: i) an exhumation path related to an overall cooling, ii) a drastic change
27
28 808 to transcurrent tectonics associated with hydrogeological connections at depth favouring the ascent
29
30 809 of hot hydrothermal fluids and, iii) the involvement of two types of secondary brines, an input from
31
32 810 the deep reservoir involving Triassic evaporites and a more recent input from the Messinian at the
33
34 811 surface, which might have caused the migration and concentration of elements of economic interest.
35
36 812 The interference between these factors influenced the redox conditions within the upper brittle
37
38 813 reservoir, leading to an alternation of oxidizing and reducing conditions that controlled the
39
40 814 formation of Fe-rich minerals ((siderite?) hematite, then siderite-pyrite). The deep penetration of
41
42 815 late-stage oxidizing Messinian secondary brines is related to the crystallization of barite. This
43
44 816 process reflects the existence of large convection cells extending from the surface to deep aquifers,
45
46 817 associated with transtensional tectonics and local heat flow, which are presumed to be related to
47
48 818 Miocene magmatism at depth.
49
50
51
52

53 819 **Acknowledgments**

54
55
56 820 The authors thank M.-C. Caumon-Jodin (GeoRessources, Vandœuvre-lès-Nancy) for Raman
57
58 821 spectroscopy analyses and T. Rigaudier (CRPG, Vandœuvre-lès-Nancy) for isotopic analyses. We
59
60

1
2 822 also thank A. Flammang and C. Demeurie who prepared thin and thick sections. Special thanks to
3
4 823 C. Montenat for stimulating discussions on the geology and metallogeny of the Betic Cordillera.
5
6 824 The authors also thank Michael Carpenter for his professional English language review. This work
7
8 825 was supported by the Ministry of Higher Education and Research (MESR, France) and the CNRS
9
10 826 ST-INSU-CT5 programme.
11
12
13 827
14
15
16
17
18
19
20
21
22
23
24
25
26
27
28
29
30
31
32
33
34
35
36
37
38
39
40
41
42
43
44
45
46
47
48
49
50
51
52
53
54
55
56
57
58
59
60

Draft Copy

- 1
2 828 Alvado, J. C. (1986). Sédimentation, déformation et manifestation magmatiques associées au
3 829 couloir de décrochement de Palomares : le bassin de Vera (SE de l'Espagne). Université de
4 830 Paris.
- 5 831 Álvarez-Valero, A. M. & Kriegsman, L. M. (2008). Partial crustal melting beneath the Betic
6 832 Cordillera (SE Spain): The case study of Mar Menor volcanic suite. *Lithos*, **101**, 379-396.
- 7 833 Álvarez, F. & Aldaya, F. (1985). Las unidades de la zona Bética en la región de Águilas-Mazarrón
8 834 (Prov. de Murcia). *Estudios Geológicos*, **41(3)**, 139-146.
- 9 835 Arribas, A. Cunningham, C. G. Rytuba, J. J. Rye, R. O. Kelly, W. C. Podwyssocki, M. H. Mckee, E. H.
10 836 & Tosdal, R. M. (1995). Geology, geochronology, fluid inclusions, and isotope
11 837 geochemistry of the Rodalquilar gold alunite deposit, Spain. *Economic Geology*, **90**, 795-
12 838 822.
- 13 839 Arribas, A. Espinosa, J. & Moro, M. C. (1983). Distribucion de elementos en trazas en las esfaleritas
14 840 y galenas de las mineralizaciones españolas asociadas con rocas volcánicas. *Tecniterrae*, **55**,
15 841 12-40.
- 16 842 Augier, R. (2004). Evolution tardi-orogénique des Cordillères bétiques (Espagne): Apports d'une
17 843 étude intégrée. PhD, Université de Pierre et Marie Curie.
- 18 844 Augier, R. Agard, P. Monie, P. Jolivet, L. Robin, C. & Booth-Rea, G. (2005a). Exhumation, doming
19 845 and slab retreat in the Betic Cordillera (SE Spain): In situ $^{40}\text{Ar}/^{39}\text{Ar}$ ages and P-T-d-t
20 846 paths for the Nevado-Filabride complex. *Journal of Metamorphic Geology*, **23**, 357-381.
- 21 847 Augier, R. Booth-Rea, G. Agard, P. Martinez-Martinez, J. M. Jolivet, L. & Azanon, J. M. (2005b).
22 848 Exhumation constraints for the lower Nevado-Filabride Complex (Betic Cordillera, SE
23 849 Spain): a Raman thermometry and Tweek multiequilibrium thermobarometry approach.
24 850 *Bulletin de la Societe Geologique de France*, **176**, 403-416.
- 25 851 Augier, R. Jolivet, L. & Robin, C. (2005c). Late Orogenic doming in the eastern Betic Cordilleras:
26 852 Final exhumation of the Nevado-Filabride complex and its relation to basin genesis.
27 853 *Tectonics*, **24**, 1-19.
- 28 854 Bakker, H. E. Jong, K. D. Helmers, H. & Biermann, C. (1989). The geodynamic evolution of the
29 855 Internal Zone of the Betic Cordilleras (south-east Spain): a model based on structural
30 856 analysis and geothermobarometry. *Journal of Metamorphic Geology*, **7**, 359-381.
- 31 857 Bakker, R. J. (1997). Clathrates: Computer programs to calculate fluid inclusion V-X properties
32 858 using clathrate melting temperatures. *Computers and Geosciences*, **23**, 1-18.
- 33 859 Bakker, R. J. (1999). Adaptation of the Bowers and Helgeson (1983) equation of state to the H₂O-
34 860 CO₂-CH₄-N₂-NaCl system. *Chemical Geology*, **154**, 225-236.
- 35 861 Bakker, R. J. (2003). Package FLUIDS 1. Computer programs for analysis of fluid inclusion data
36 862 and for modelling bulk fluid properties. *Chemical Geology*, **194**, 3-23.
- 37 863 Bakker, R. J. & Jansen, J. B. H. (1990). Preferential water leakage from fluid inclusions by means
38 864 of mobile dislocations. *Nature*, **345**, 58-60.
- 39 865 Bakker, R. J. & Jansen, J. B. H. (1994). A mechanism for preferential H₂O leakage from fluid
40 866 inclusions in quartz, based on TEM observations. *Contributions to Mineralogy and
41 867 Petrology*, **116**, 7-20.
- 42 868 Banks, D. A. Da Vies, G. R. Yardley, B. W. D. Mccaig, A. M. & Grant, N. T. (1991). The chemistry
43 869 of brines from an Alpine thrust system in the Central Pyrenees: An application of fluid
44 870 inclusion analysis to the study of fluid behaviour in orogenesis. *Geochimica et
45 871 Cosmochimica Acta*, **55**, 1021-1030.
- 46 872 Banks, D. A. Giuliani, G. Yardley, B. W. D. & Cheilletz, A. (2000). Emerald mineralisation in
47 873 Colombia: fluid chemistry and the role of brine mixing. *Mineralium Deposita*, **35**, 699-713.
- 48 874 Beaudoin, G. (1994). Evidence for an upper crustal source for gold in the Ag-Pb-Zn-Au veins of the
49 875 Kokanee Range, British Columbia. *Economic Geology*, **89**, 397-400.
- 50 876 Bellon, H. Bordet, P. & Montenat, C. (1983). Chronologie du magmatisme néogène des Cordillères
51 877 bétiques (Espagne méridionale). *Bulletin de la Societe Geologique de France*, **25**, 205-217.

- 1 878 Benito, R.Lopez-Ruiz, J.Cebria, J. M.Hertogen, J.Doblas, M.Oyarzun, R. & Demaiffe, D. (1999).
2 879 Sr and O isotope constraints on source and crustal contamination in the high-K calc-alkaline
3 880 and shoshonitic neogene volcanic rocks of SE Spain. *Lithos*, **46**, 773-802.
- 4 881 Beyssac, O.Bollinger, L.Avouac, J.-P. & Goffé, B. (2004). Thermal metamorphism in the lesser
5 882 Himalaya of Nepal determined from Raman spectroscopy of carbonaceous material. *Earth
6 883 and Planetary Science Letters*, **225**, 233-241.
- 7 884 Beyssac, O.Goffé, B.Chopin, C. & Rouzaud, J. N. (2002). Raman spectra of carbonaceous material
8 885 in metasediments: A new geothermometer. *Journal of Metamorphic Geology*, **20**, 859-871.
- 9 886 Beyssac, O. & Lazzari, M. (2012). Application of Raman spectroscopy to the study of graphitic
10 887 carbons in the Earth Sciences. *EMU Notes in Mineralogy*, **12**, 415-454.
- 11 888 Bezada, M.-J.Humphreys, E.-D.Toomey, D.-R.Harnafi, M.Dávila, J.-M. & Gallart, J. (2013).
12 889 Evidence for slab rollback in westernmost mediterranean from improved upper mantle
13 890 imaging. *Earth and Planetary Science Letters*, **368**, 51-60.
- 14 891 Bodnar, R. J. (2003). Introduction to aqueous-electrolyte fluid inclusions. In: Iain Samson, A. A. A.
15 892 D. M. (ed.) *Fluid Inclusions : Analysis and Interpretation*. Robert Raeside ed. Vancouver,
16 893 British Columbia: Mineralogical Association of Canada.
- 17 894 Böhlke, J. K. & Irwin, J. J. (1992). Laser microprobe analyses of noble gas isotopes and halogens in
18 895 fluid inclusions: Analyses of microstandards and synthetic inclusions in quartz. *Geochimica
19 896 et Cosmochimica Acta*, **56**, 187-201.
- 20 897 Boiron, M.-C.Cathelineau, M.Banks, D. A.Fourcade, S. & Vallance, J. (2003). Mixing of
21 898 metamorphic and surficial fluids during the uplift of the Hercynian upper crust:
22 899 consequences for gold deposition. *Chemical Geology*, **194**, 119-141.
- 23 900 Bolze, J.Ott D'estevou, P.Bordet, P.Montenat, C. & De Larouzière, F. (1986). Processus thermo-
24 901 mécaniques associés à l'évolution des bassins néogènes des Bétiques internes orientales
25 902 (Espagne Sud-Est). **Rapport interne n°35**, 92p.
- 26 903 Booth-Rea, G.Azañón, J.-M.Azor, A. & García-Dueñas, V. (2004). Influence of strike-slip fault
27 904 segmentation on drainage evolution and topography. A case study: the Palomares Fault
28 905 Zone (southeastern Betics, Spain). *Journal of Structural Geology*, **26**, 1615-1632.
- 29 906 Booth-Rea, G.Azañón, J. M.García-Dueñas, V. & Augier, R. (2003). Uppermost Tortonian to
30 907 Quaternary depocentre migration related with segmentation of the strike-slip Palomares
31 908 Fault Zone, Vera Basin (SE Spain). *Comptes Rendus Geosciences*, **335**, 751-761.
- 32 909 Bottrell, S. H.Yardley, B. W. D. & Buckley, F. (1988). A modified crush-leach method for the
33 910 analysis of fluid inclusion electrolytes. *Bull. Minéral.*, **111**, 279-290.
- 34 911 Boullier, A.-M. (1999). Fluid inclusions: tectonic indicators. *Journal of Structural Geology*, **21**,
35 912 1229-1235.
- 36 913 Bourillot, R.Vennin, E.Rouchy, J.-M.Durlet, C.Rommevaux, V.Kolodka, C. & Knap, F. (2009).
37 914 Structure and evolution of a Messinian mixed carbonate-siliciclastic platform: the role of
38 915 evaporites (Sorbas Basin, South-east Spain). *Sedimentology*, **57**, 477-512.
- 39 916 Bowers, T. S. & Helgeson, H. C. (1983). Calculation of the thermodynamic and geochemical
40 917 consequences of nonideal mixing in the system H₂O-CO₂-NaCl on phase relations in
41 918 geologic systems: Equation of state for H₂O-CO₂-NaCl fluids at high pressures and
42 919 temperatures. *Geochimica et Cosmochimica Acta*, **47**, 1247-1275.
- 43 920 Carrillo-Rosúa, F.-J.Morales-Ruano, S.Esteban-Arispe, I. & Hach-Ali, P. F. (2009). Significance of
44 921 phyllosilicate mineralogy and mineral chemistry in an epithermal environment. Insights
45 922 from the Palai-Islica Au-Cu deposit (Almer-Áa, SE Spain). *Clays and Clay Minerals*, **57**, 1-
46 923 24.
- 47 924 Carrillo-Rosúa, F.-J.Morales-Ruano, S.Fenoll Hach-Ali, P.Boyce, A.-J. & Fallick, A.-E. (2003).
48 925 Génesis de la barita de Las Herrerías y Sierra Almagrera. *Boletín de la Sociedad Española
49 926 de Mineralogía*, **26-A**, 159-160.
- 50 927 Carrillo-Rosúa, F.-J.Morales Ruano, S. & Fenoll Hach-Ali, P. (2002). The three generations of gold
51 928 in the Palai-Islica epithermal deposit, southeastern Spain. *Canadian Mineralogist*, **40**, 1465-
52 929 1481.

- 1
2 930 Cathelineau, M.Boiron, M. C.Essarraj, S.Dubessy, J.Lespinasse, M. & Poty, B. (1993). Fluid
3 931 pressure variations in relation to multistage deformation and uplift; a fluid inclusion study of
4 932 Au quartz veins. *European Journal of Mineralogy*, **5**, 107-121.
- 5 933 Cesare, B.Rubatto, D. & Gómez-Pugnaire, M. (2009). Do extrusion ages reflect magma generation
6 934 processes at depth? An example from the Neogene Volcanic Province of SE Spain.
7 935 *Contributions to Mineralogy and Petrology*, **157**, 267-279.
- 8 936 Clauzon, G. (1980). Révision de l'interprétation géodynamique du passage Miocène - Pliocène dans
9 937 le bassin de Vera (Espagne méridionale) : les coupes d'Antas et de Cuevas del Almanzora.
10 938 *Rivista Italiana di Paleontologia*, **86**, 203-214.
- 11 939 Clauzon, G.Suc, J.-P.Gautier, F.Berger, A. & Loutre, M.-F. (1996). Alternate interpretation of the
12 940 Messinian salinity crisis: Controversy resolved? *Geology*, **24**, 363-366.
- 13 941 Claypool, G. E.Holser, W. T.Kaplan, I. R.Sakai, H. & Zak, I. (1980). The age curves of sulfur and
14 942 oxygen isotopes in marine sulfate and their mutual interpretation. *Chemical Geology*, **28**,
15 943 199-260.
- 16 944 Clayton, R. N. & Mayeda, T. K. (1963). The use of bromine pentafluoride in the extraction of
17 945 oxygen from oxides and silicates for isotopic analysis. *Geochimica et Cosmochimica Acta*,
18 946 **27**, 43-52.
- 19 947 Conticelli, S.Guarnieri, L.Farinelli, A.Mattei, M.Avanzinelli, R.Bianchini, G.Boari, E.Tommasini,
20 948 S.Tiepolo, M.Prelevic, D. & Venturelli, G. (2009). Trace elements and Sr-Nd-Pb isotopes of
21 949 K-rich, shoshonitic, and calc-alkaline magmatism of the Western Mediterranean Region:
22 950 Genesis of ultrapotassic to calc-alkaline magmatic associations in a post-collisional
23 951 geodynamic setting. *Lithos*, **107**, 68-92.
- 24 952 Crespo-Blanc, A.Orozco, M. & Garcia-Dueñas, V. (1994). Extension versus compression during the
25 953 Miocene tectonic evolution of the Betic chain. Late folding of normal fault systems.
26 954 *Tectonics*, **13**, 78-88.
- 27 955 De Jong, K. (1991). Tectono-metamorphic studies and radiometric dating in the Betic Cordilleras
28 956 (SE Spain). Vrije Universiteit.
- 29 957 De Jong, K. (2003). Very fast exhumation of high-pressure metamorphic rocks with excess ⁴⁰Ar
30 958 and inherited ⁸⁷Sr, Betic Cordilleras, southern Spain. *Lithos*, **70**, 91-110.
- 31 959 Demoustier, A.Castroviejo, R. & Charlet, J.-M. (1998). Clasificación textural del cuarzo epitermal
32 960 (Au-Ag) de relleno filoniano del área volcánica de Cabo de Gata, Almería. *Boletín*
33 961 *Geológico y Minero*, **109**, 449-468.
- 34 962 Diamond, L.Tarantola, A. & Stünitz, H. (2010). Modification of fluid inclusions in quartz by
35 963 deviatoric stress. II: experimentally induced changes in inclusion volume and composition.
36 964 *Contributions to Mineralogy and Petrology*.
- 37 965 Dubessy, J. (1984). Simulation des équilibres chimiques dans le système C-O-H. Conséquences
38 966 méthodologiques pour les inclusions fluides. *Bull. Minéral.*, **107**, 155-168.
- 39 967 Dublyansky, Y. V. & Spötl, C. (2009). Hydrogen and oxygen isotopes of water from inclusions in
40 968 minerals: design of a new crushing system and on-line continuous-flow isotope ratio mass
41 969 spectrometric analysis. *Rapid Commun Mass Spectrom*, **23**.
- 42 970 Duggen, S.Hoernle, K.Van Den Bogaard, P. & Garbe-Schonberg, D. (2005). Post-Collisional
43 971 Transition from Subduction- to Intraplate-type Magmatism in the Westernmost
44 972 Mediterranean: Evidence for Continental-Edge Delamination of Subcontinental Lithosphere.
45 973 *Journal of Petrology*, **46**, 1155-1201.
- 46 974 Duggen, S.Hoernle, K.Van Den Bogaard, P. & Harris, C. (2004). Magmatic evolution of the
47 975 Alboran region: The role of subduction in forming the western Mediterranean and causing
48 976 the Messinian Salinity Crisis. *Earth and Planetary Science Letters*, **218**, 91-108.
- 49 977 Egeler, C. G. & Simon, O. J. (1969). «Sur la tectonique de la Zone Bétique (Cordillères Bétiques,
50 978 Espagne). Etudes basées sur la recherche dans le secteur compris entre Almería y Vélez-
51 979 Rubio». *Verk. Kon. Ned. Akad. V. Wetensch Afd. Nat. serts. reeks.*, **25**, 90 p.
- 52 980 Essarraj, S.Boiron, M.-C.Cathelineau, M.Banks, D. A. & Benharref, M. (2005). Penetration of
53 981 surface-evaporated brines into the Proterozoic basement and deposition of Co and Ag at Bou
54
55
56
57
58
59
60

- 1 982 Azzer (Morocco): Evidence from fluid inclusions. *Journal of African Earth Sciences*, **41**,
2 983 25-39.
- 3 984 Esteban-Arispe, I.Carrillo-Rosúa, J.Morales-Ruano, S.Velasco-Roldán, F. & Boyce, A.-J.
4 985 Mineralogy and fluid evolution of Pb-Zn-Cu(Ag-Au) epithermal veins in San José (Almería,
5 986 Southeastern Spain). Proceedings of the XX European Current Research on Fluid
6 987 Inclusions, 2009. Fluid and Melt Inclusions: using bubbles to decode the Earth., 79 - 80.
- 7 988 Famin, V.Hébert, R.Philippot, P. & Jolivet, L. (2005). Ion probe and fluid inclusion evidence for
8 989 co-seismic fluid infiltration in a crustal detachment. *Contributions to Mineralogy and
9 990 Petrology*, **150**, 354-367.
- 10 991 Famin, V. & Nakashima, S. (2004). Fluid migration in fault zones and the evolution of
11 992 detachments: The example of Tinos Island (Greece). In: Universal Academy Press, I. (ed.)
12 993 *Physicochemistry of Water in Geological and Biological Systems*. Tokyo, Japan.
- 13 994 Field, C. W. & Fifarek, R. H. (1985). Light stable isotope systematics in the epithermal
14 995 environment In: Berger, B. R., and Bethke, P.M. (ed.) *Geology and Geochemistry of
15 996 Epithermal Systems, Reviews in Economic Geology*.
- 16 997 Fontes, J. C. & Matray, J. M. (1993). Geochemistry and origin of formation brines from the Paris
17 998 Basin, France: 1. Brines associated with Triassic salts. *Chemical Geology*, **109**, 149-175.
- 18 999 Fortuin, A. R.Kelling, J. M. D. & Roep, T. B. (1995). The enigmatic Messinian-Pliocene section of
19 1000 Cuevas del Almanzora (Vera Basin, SE Spain) revisited-erosional features and strontium
20 1001 isotope ages. *Sedimentary Geology*, **97**, 177-201.
- 21 1002 Garcés, M.Krijgsman, W. & Agusti, J. (1998). Chronology of the late Turolian deposits of the
22 1003 Fortuna basin (SE Spain): implications for the Messinian evolution of the eastern Betics.
23 1004 *Earth and Planetary Science Letters*, **163**, 69-81.
- 24 1005 Gargani, J.Moretti, I. & Letouzey, J. (2008). Evaporite accumulation during the Messinian Salinity
25 1006 Crisis: The Suez Rift case. *Geophysical Research Letters*, **35**, L02401.
- 26 1007 Gautier, F.Clauzon, G.Suc, J. P.Cravatte, J. & Violanti, D. (1994). Age and duration of the
27 1008 Messinian salinity crisis. *Comptes Rendus de l'Académie des Sciences, Series IIA, Earth and
28 1009 Planetary Science*, **318**, 1103-1109.
- 29 1010 Giesemann, A.Jaeger, H. J.Norman, A. L.Krouse, H. R. & Brand, W. A. (1994). Online Sulfur-
30 1011 Isotope Determination Using an Elemental Analyzer Coupled to a Mass Spectrometer.
31 1012 *Analytical Chemistry*, **66**, 2816-2819.
- 32 1013 Gomez-Pugnaire, M. T. & Fernandez-Soler, J. M. (1987). High-pressure metamorphism in
33 1014 metabasites from the Betic Cordilleras (S.E. Spain) and its evolution during the Alpine
34 1015 orogeny. *Contributions to Mineralogy and Petrology*, **95**, 231-244.
- 35 1016 Gomez-Pugnaire, M. T.Galindo-Zaldivar, J.Rubatto, D.Gonzalez-Lodeiro, F.Lopez Sanchez-
36 1017 Vizcaino, V. & Jabaloy, A. (2004). A reinterpretation of the Nevado-Filabride and
37 1018 Alpujarride Complexes (Betic Cordillera): Field, petrography and U-Pb ages from
38 1019 orthogneisses (western Sierra Nevada, S Spain). *Schweizerische Mineralogische und
39 1020 Petrographische Mitteilungen*, **84**, 303-322.
- 40 1021 Gomez-Pugnaire, M. T.Rubatto, D.Fernandez-Soler, J. M.Jabaloy, A.Lopez-Sanchez-Vizcaino,
41 1022 V.Gonzalez-Lodeiro, F.Galindo-Zaldivar, J. & Padron-Navarta, J. A. (2012). Late Variscan
42 1023 magmatism in the Nevado-Filabride Complex: U-Pb geochronologic evidence for the pre-
43 1024 Mesozoic nature of the deepest Betic complex (SE Spain). *Lithos*, **146-147**, 93-111.
- 44 1025 Graeser, S. & Friedrich, G. (1970). Zur Frage der Alterstellung und Genese der Blei-Zink-
45 1026 Vorkommen der Sierra de Cartagena in Spanien. *Mineralium Deposita*, **5**, 365-374.
- 46 1027 Griveaud, P.Coppier, G.Montenat, C. & Ott D'estevou, P. (1990). Le Néogène des sierras
47 1028 d'Aguilas. In: Montenat, C. (ed.) *Les bassins néogènes du domaine Bétique oriental
48 1029 (Espagne)*. Doc.et Trav. IGAL ed. Paris.
- 49 1030 Hernandez, J.De Larouziere, F. D.Bolze, J. & Bordet, P. (1987). Le magmatisme neogene betico-
50 1031 rifain et le couloir de décrochement trans-Alboran. *Bulletin de la Societe Geologique de
51 1032 France*, **III**, 257-267.

- 1
2 1033 Hollister, L. (1990). Enrichment of CO₂ in fluid inclusions in quartz by removal of H₂O during
3 1034 crystal-plastic deformation. *Journal of Structural Geology*, **12**, 895-901.
- 4 1035 Huizenga, J. M. (2001). Thermodynamic modelling of C-O-H fluids. *Lithos*, **55**, 101-114.
- 5 1036 Huizenga, J. M. (2011). Thermodynamic modelling of a cooling C-O-H fluid-graphite system:
6 1037 implications for hydrothermal graphite precipitation. *Mineralium Deposita*, **46**, 23-33.
- 7 1038 Ingebritsen, S. E. & Manning, C. E. (2002). Diffuse fluid flux through orogenic belts: Implications
8 1039 for the world ocean. *Proceedings of the National Academy of Sciences USA*, **99**, 9,113-
9 1040 9,116.
- 10 1041 Jabaloy, A.Galindo-Zaldívar, J. & González-Lodeiro, F. (1993). The Alpujarride-Nevado-Fibábride
11 1042 extensional shear zone, Betic Cordillera, SE Spain. *Journal of Structural Geology*, **15**, 555-
12 1043 569.
- 13 1044 Jessell, M. W. (1987). Grain-boundary migration microstructures in a naturally deformed quartzite.
14 1045 *Journal of Structural Geology*, **9**, 1007-1014.
- 15 1046 Johnson, E. L. & Hollister, L. S. (1995). Syndeformational fluid trapping in quartz: determining the
16 1047 pressure- temperature conditions of deformation from fluid inclusions and the formation of
17 1048 pure CO₂ fluid inclusions during grain-boundary migration. *Journal of Metamorphic
18 1049 Geology*, **13**, 239-249.
- 19 1050 Jolivet, L.Augier, R.Faccenna, C.Negro, F.Rimmele, G.Agard, P.Robin, C.Rossetti, F. & Crespo-
20 1051 Blanc, A. (2008). Subduction, convergence and the mode of backarc extension in the
21 1052 Mediterranean region. *Bulletin de la Societe Geologique de France*, **179**, 525-550.
- 22 1053 Kerrich, R. (1976). Some effects of tectonic recrystallisation on fluid inclusions in vein quartz.
23 1054 *Contributions to Mineralogy and Petrology*, **59**, 195-202.
- 24 1055 Krantz, R. L. (1983). Microcracks in rocks: a review. *Tectonophysics*, **100**, 449-480.
- 25 1056 Krijgsman, W.Garcés, M.Agusti, J.Raffi, I.Taberner, C. & Zachariasse, W. J. (2000). The
26 1057 "Tortonian salinity crisis" of the eastern Betics (Spain). *Earth and Planetary Science
27 1058 Letters*, **181**, 497-511.
- 28 1059 Krijgsman, W.Hilgen, F. J.Raffi, I.Sierro, F. J. & Wilson, D. S. (1999). Chronology, causes and
29 1060 progression of the Messinian salinity crisis. *Nature*, **400**, 652-655.
- 30 1061 Leisen, M.Boiron, M.-C.Richard, A. & Dubessy, J. (2012a). Determination of Cl and Br
31 1062 concentrations in individual fluid inclusions by combining microthermometry and LA-
32 1063 ICPMS analysis: Implications for the origin of salinity in crustal fluids. *Chemical Geology*,
33 1064 **330-331**, 197-206.
- 34 1065 Leisen, M.Dubessy, J.Boiron, M.-C. & Lach, P. (2012b). Improvement of the determination of
35 1066 element concentrations in quartz-hosted fluid inclusions by LA-ICP-MS and Pitzer
36 1067 thermodynamic modeling of ice melting temperature. *Geochimica et Cosmochimica Acta*,
37 1068 **90**, 110-125.
- 38 1069 Lespinasse, M. (1999). Are fluid inclusion planes useful in structural geology? *Journal of
39 1070 Structural Geology*, **21**, 1237-1243.
- 40 1071 Lespinasse, M.Désindes, L.Fratczak, P. & Petrov, V. (2005). Microfissural mapping of natural
41 1072 cracks in rocks: Implications for fluid transfers quantification in the crust. *Chemical
42 1073 Geology*, **223**, 170-178.
- 43 1074 Lister, G. S. & Davis, G. A. (1989). The origin of metamorphic core complexes and detachment
44 1075 faults formed during Tertiary continental extension in the northern Colorado River region,
45 1076 U.S.A. *Journal of Structural Geology*, **11**, 65-94.
- 46 1077 Lonergan, L. & Mange-Rajetzky, M. A. (1994). Evidence for Internal Zone unroofing from
47 1078 foreland basin sediments, Betic Cordillera, SE Spain. *Journal of the Geological Society*,
48 1079 **151**, 515-529.
- 49 1080 Lonergan, L. & White, N. (1997). Origin of the Betic-Rif mountain belt. *Tectonics*, **16**, 504-522.
- 50 1081 Lopez Ruiz, J. & Rodriguez Badiola, E. (1980). La region volcanica neogena del sureste de Espana.
51 1082 *Estudios Geologicos*, **36**, 5-63.
- 52 1083 Manning, C. E. & Ingebritsen, S. E. (1999). Permeability of the continental crust: The implications
53 1084 of geothermal data and metamorphic systems. *Reviews of Geophysics*, **37**, 127-150.

- 1 1085 Martínez-Frías, J. (1998). An ancient Ba-Sb-Ag-Fe-Hg-bearing hydrothermal system in SE Spain.
2 1086 *Episodes*, **21**, 248-251.
- 3 1087 Martínez-Frías, J., Delgado-Huertas, A., García-Moreno, F., Reyes, E., Lunar, R. & Rull, F. (2007).
4 1088 Isotopic signatures of extinct low-temperature hydrothermal chimneys in the Jaroso Mars
5 1089 analog. *Planetary and Space Science*, **55**, 441-448.
- 6 1090 Martínez-Martínez, J. M. & Azañón, J. M. (2002). Orthogonal extension in the hinterland of the
7 1091 Gibraltar Arc (Betics, SE Spain), in Reconstruction of the evolution of the Alpine-
8 1092 Himalayan Orogen. *Journal of the Virtual Explorer*, **8**, 3-22.
- 9 1093 Martínez-Martínez, J. M., Soto, J. I. & Balanya, J. C. (2002). Orthogonal folding of extensional
10 1094 detachments: Structure and origin of the Sierra Nevada elongated dome (Betics, SE Spain).
11 1095 *Tectonics*, **21**.
- 12 1096 Martínez-Frías, J., García Guinea, J., López Ruiz, J., López García, J. Á. & Benito García, R. (1989).
13 1097 Las mineralizaciones epitermales de Sierra Almagrera y de la cuenca de Herrerías,
14 1098 Cordilleras Béticas. *Bol. Soc. Esp. Mineral.*, **12**, 261-271.
- 15 1099 Massonne, H.-J. & Schreyer, W. (1987). Phengite geobarometry based on the limiting assemblage
16 1100 with K-feldspar, phlogopite, and quartz. *Contributions to Mineralogy and Petrology*, **96**,
17 1101 212-224.
- 18 1102 Mccaig, A. M., Tritlla, J. & Banks, D. A. (2000). Fluid mixing and recycling during Pyrenean
19 1103 thrusting: evidence from fluid inclusion halogen ratios. *Geochimica et Cosmochimica Acta*,
20 1104 **64**, 3395-3412.
- 21 1105 Menzies, C. D., Teagle, D. A. H., Craw, D., Cox, S. C., Boyce, A. J., Barrie, C. D. & Roberts, S. (2014).
22 1106 Incursion of meteoric waters into the ductile regime in an active orogen. *Earth and*
23 1107 *Planetary Science Letters*, **399**, 1-13.
- 24 1108 Montenat, C. & Ott D'estevou, P. (1990). Eastern Betic Neogene basins-a review. *D.E.T.I.s (Ed.) :*
25 1109 *Les bassins néogènes de domaines bétique oriental (Espagne)*, **12-13**, 9-15.
- 26 1110 Montenat, C., Ott D'estevou, P., De Larouzière, F. & Bedu, P. (1987). Originalité géodynamique des
27 1111 bassins néogènes de domaine oriental (Espagne). *Extrait de "Notes et Mémoires"*, **21**.
- 28 1112 Morales Ruano, S. (1994). Mineralogía, geoquímica y metalogénia de los yacimientos
29 1113 hidrotermales del sureste de España (Aguilas-Sierra Almagrera). Universidad de Granada.
- 30 1114 Morales Ruano, S., Both, R. & Fenoll Hach-Ali, P. (1993). Paragenesis and regional zoning of the
31 1115 polymetallic ore deposits in the Aguilas and Sierra Almagrera-Herrerías areas, Southeastern
32 1116 Spain. 171-174.
- 33 1117 Morales Ruano, S., Both, R. & Fenoll Hach-Ali, P. (1995). Fluid evolution and mineral deposition in
34 1118 the Aguilas – Sierra Almagrera base metal ores, southeastern Spain. *Mineral Deposits*, 365-
35 1119 368.
- 36 1120 Morales Ruano, S., Rosua, F. J., C. Hach-Ali, P., F. Chacon, F. D. L. F. & Lopez, E. C. (2000).
37 1121 Epithermal Cu-Au mineralization in the Palai-Islica deposit, Almería, southeastern Spain:
38 1122 Fluid-inclusion evidence for mixing of fluids as a guide to gold mineralization. *Canadian*
39 1123 *Mineralogist*, **38**, 553-565.
- 40 1124 Morrison, J. & Anderson, J. L. (1998). Footwall refrigeration along a detachment fault: implications
41 1125 for thermal evolution of core complexes. *Science*, **279**, 63-66.
- 42 1126 Mulch, A., Teyssier, C., Cosca, M., Vanderhaeghe, O. & Vennemann, T. (2004). Reconstructing
43 1127 paleoelevation in eroded orogens. *Geology*, **32**, 525-528.
- 44 1128 Oen, I. S., Fernández, J. C. & Manteca, J. I. (1975). The lead-zinc and associated ores of La Unión-
45 1129 Sierra de Cartagena, Spain. *Economic Geology*, **70**, 1259-1278.
- 46 1130 Omodeo Salé, S., Gennari, R., Lugli, S., Manzi, V. & Roveri, M. (2012). Tectonic and climatic control
47 1131 on the Late Messinian sedimentary evolution of the Nijar Basin (Betic Cordillera, Southern
48 1132 Spain). *Basin Research*, **24**, 314-337.
- 49 1133 Passchier, C. W. & Trouw, R. A. J. (2005). Microtectonics.
- 50 1134 Pedrera, A., Galindo-Zaldívar, J., Tello, A. & Marin-Lechado, C. (2010). Intramontane basin
51 1135 development related to contractional and extensional structure interaction at the termination

- 1
2 1136 of a major sinistral fault: The Huerca-Overa Basin (Eastern Betic Cordillera). *Journal of*
3 1137 *Geodynamics*, **49**, 271-286.
- 4 1138 Platt, J. P. (2007). From orogenic hinterlands to Mediterranean-style back-arc basins: a comparative
5 1139 analysis. *Journal of the Geological Society*, **164**, 297-311.
- 6 1140 Platt, J. P., Anczkiewicz, R., Soto, J. I., Kelley, S. P. & Thirlwall, M. (2006). Early Miocene
7 1141 continental subduction and rapid exhumation in the western Mediterranean. *Geology*, **34**,
8 1142 981-984.
- 9 1143 Platt, J. P. & Vissers, R. L. M. (1989). Extensional collapse of thickened continental lithosphere: A
10 1144 working hypothesis for the Alboran Sea and Gibraltar arc. *Geology*, **17**, 540-543.
- 11 1145 Prelevic, D., Foley, S. F., Romer, R. & Conticelli, S. (2008). Mediterranean Tertiary lamproites
12 1146 derived from multiple source components in postcollisional geodynamics. *Geochimica et*
13 1147 *Cosmochimica Acta*, **72**, 2125-2156.
- 14 1148 Rouchy, J. M., Taberner, C., Blanc-Valleron, M.-M., Sprovieri, R., Russell, M., Pierre, C., Di Stefano,
15 1149 E., Pueyo, J. J., Caruso, A., Dinarã S-Turell, J., Gomis-Coll, E., Wolff, G. A., Cespuglio,
16 1150 G., Ditchfield, P., Pestrea, S., Combourieu-Nebout, N., Santisteban, C. & Grimalt, J. O. (1998).
17 1151 Sedimentary and diagenetic markers of the restriction in a marine basin: The Lorca Basin
18 1152 (SE Spain) during the Messinian. *Sedimentary Geology*, **121**, 23-55.
- 19 1153 Scheppard, S. & Schwarcz, H. (1970). Fractionation of carbon and oxygen isotopes and magnesium
20 1154 between coexisting metamorphic calcite and dolomite. *Contributions to Mineralogy and*
21 1155 *Petrology*, **26**, 161-198.
- 22 1156 Seidenkrantz, M. S., Kouwenhoven, T. J., Jorissen, F. J., Shackleton, N. J. & Van Der Zwaan, G. J.
23 1157 (2000). Benthic foraminifera as indicators of changing Mediterranean-Atlantic water
24 1158 exchange in the late Miocene. *Marine Geology*, **163**, 387-407.
- 25 1159 Sheppard, S. (1986). Characterization and isotopic variations in natural waters. In: Mineral., M. S.
26 1160 A. R. (ed.) *Stable Isotopes in High Temperature Geological Processes*. Washington, D.C.
- 27 1161 Siebenaller, L., Boiron, M. C., Vanderhaeghe, O., Hibsich, C., Jessell, M. W., Andre-Mayer, A. S., France-
28 1162 Lanord, C. & Photiades, A. (2013). Fluid record of rock exhumation across the brittle-
29 1163 ductile transition during formation of a Metamorphic Core Complex (Naxos Island,
30 1164 Cyclades, Greece). *Journal of Metamorphic Geology*, **31**, 313-338.
- 31 1165 Stipp, M. & Kunze, K. (2008). Dynamic recrystallization near the brittle-plastic transition in
32 1166 naturally and experimentally deformed quartz aggregates. *Tectonophysics*, **448**, 77-97.
- 33 1167 Tarantola, A., Diamond, L. & Stünitz, H. (2010). Modification of fluid inclusions in quartz by
34 1168 deviatoric stress I: experimentally induced changes in inclusion shapes and microstructures.
35 1169 *Contributions to Mineralogy and Petrology*.
- 36 1170 Tarantola, A., Diamond, L., W. Stünitz, H. A., T. & Pec, M. (2012). Modification of fluid inclusions in
37 1171 quartz by deviatoric stress III: Influence of principal stresses on inclusion density and
38 1172 orientation. *Contributions to Mineralogy and Petrology*.
- 39 1173 Tarantola, A., Mullis, J., Vennemann, T., Dubessy, J. & De Capitani, C. (2007). Oxidation of methane
40 1174 at the CH₄/H₂O-(CO₂) transition zone in the external part of the Central Alps, Switzerland:
41 1175 Evidence from stable isotope investigations. *Chemical Geology*, **237**, 329-357.
- 42 1176 Turner, S. P., Platt, J. P., George, R. M., Kelley, S. P., Pearson, D. G. & Nowell, G. M. (1999).
43 1177 Magmatism Associated with Orogenic Collapse of the Betic Alboran Domain, SE Spain.
44 1178 *Journal of Petrology*, **40**, 1011-1036.
- 45 1179 Ulrich, M. R. & Bodnar, R. J. (1988). Systematics of stretching of fluid inclusions. II. Barite at one
46 1180 atmosphere confining pressure. *Economic Geology*, **83**, 1037-1046.
- 47 1181 Van Den Kerkhof, A. M. & Hein, U. F. (2001). Fluid inclusion petrography. *Lithos*, **55**, 27-47.
- 48 1182 Vanderhaeghe, O. & Teyssier, C. (2001). Crustal-scale rheological transitions during late-orogenic
49 1183 collapse. *Tectonophysics*, **335**, 211-228.
- 50 1184 Vityk, M., Bodnar, R. J. & Dudok, I. (1995). Natural and synthetic re-equilibration textures of fluid
51 1185 inclusions in quartz (Marmarosh Diamonds): Evidence for refilling under conditions of
52 1186 compressive loading. *European Journal of Mineralogy*, **7**, 1071-1087.

- 1
2 1187 Weijermars, R. (1985). Uplift history of a Betic fold nappe inferred from Neogene- Quaternary
3 1188 sedimentation and tectonics (in the Sierra Alhamilla and Almeria, Sorbas and Tabernas
4 1189 basins of the Betic Cordilleras, SE Spain. *Geologie en Mijnbouw*, **64**, 397-411.
5 1190 Wernicke, B. & Burchfiel, B. C. (1982). Modes of extensional tectonics. *Journal of Structural*
6 1191 *Geology*, **4**, 105-115.
7 1192 Westra, G. (1969). Petrogenesis of a composite metamorphic facies series in an intricate fault zone
8 1193 of the southeastern Sierra Cabrera (SE, Spain). PhD, Amsterdam.
9 1194 Wilkins, R. W. T. & Barkas, J. P. (1978). Fluid inclusions, deformation and recrystallization in
10 1195 granite tectonites. *Contributions to Mineralogy and Petrology*, **65**, 293-299.
11 1196 Yardley, B. W. D. (2005). 100th Anniversary Special Paper: Metal Concentrations in Crustal Fluids
12 1197 and Their Relationship to Ore Formation. *Economic Geology*, **100**, 613-632.
13 1198 Zeck, H. P. Maluski, H. & Kristensen, A. B. (2000). Revised geochronology of the Neogene calc-
14 1199 alkaline volcanic suite in Sierra de Gata, Alborán volcanic province, SE Spain. *Journal of*
15 1200 *the Geological Society, London*, **157**, 75-81.
16 1201 Zhang, Y.-G. & Frantz, J. D. (1987). Determination of the homogenization temperatures and
17 1202 densities of supercritical fluids in the system NaClKClCaCl₂H₂O using synthetic fluid
18 1203 inclusions. *Chemical Geology*, **64**, 335-350.
19 1204 Zheng, Y.-F. (1993). Calculation of oxygen isotope fractionation in anhydrous silicate minerals.
20 1205 *Geochimica et Cosmochimica Acta*, **57**, 1079-1091.
21 1206
22 1207

23
24
25 1208 Figure 1: a) Geological context of the Eastern Betics and location of the Sierra Almagrera (modified after Augier
26 1209 (2004)). b) Geological map of the Sierra Almagrera, Vera basin and Palomares fault zone (modified after Booth-Rea
27 1210 (2004) and Montenat & Ott D'estevou (1990), and location of sampling areas. c) Poles of mineralized V-ore veins
28 1211 (barite and siderite) in El Arteal tunnel represented on lower-hemisphere stereogram.

29 1212
30
31
32 1213 Figure 2: a) V-Qtz1 quartz vein parallel to the rock foliation. b) Optical microphotograph under cross-polarized light
33 1214 (XPL) showing petrography of Qtz1: static recrystallization (120° angles) and grain boundary migration
34 1215 recrystallization. c) Qtz1: recrystallised quartz with transgranular FIP. d) Qtz1-tg1 FIP. e) Qtz1-tg2 FIP. f) Pole
35 1216 projections of Qtz1-tg1 and Qtz1-tg2 fluid inclusion planes represented on lower hemisphere stereogram. Arrows
36 1217 indicate the directions of opening. L for liquid, V for vapour and S for solid.

37 1218
38 1219 Figure 3: a) V-Qtz2 quartz vein locally parallel to the foliation (upper part), while the main section is discordant to the
39 1220 foliation (central part). b) Relationship between petrography of recrystallised quartz (subgrain rotation and bulging) and
40 1221 fluid inclusions. c) Optical microphotographs under plane-polarized light showing intragranular Qtz2-ig. d) Deformed
41 1222 fluid inclusion Qtz2-ig. e) Pole projections of Qtz2-ig fluid inclusion planes represented on lower-hemisphere
42 1223 stereogram.

43 1224
44
45 1225 Figure 4: a) N10E V-Qtz2 discordant to the foliation reopened as V-Qtz3, intersected by V-ore discordant vein. Optical
46 1226 microphotographs under natural light: b) Contact between Qtz2 and Qtz3. Qtz2 grains still showing undulose extinction
47 1227 and affected by Qtz2-tg. Qtz3 euhedral quartz containing only Qtz3-p primary fluid inclusions. Hematite microfissures
48 1228 affecting Qtz2. Hematite also filling open spaces between Qtz3 crystals. c) Zoom of zone localized in b). d) Hematite in
49 1229 reflected light. e) Qtz2-tg. f) Qtz3-p.

50 1230
51
52
53 1231 Figure 5: Optical microphotographs of V-ore and related minerals, in plane-polarized light (PPL), cross-polarized light
54 1232 (XPL) and reflected light (RL). a) Vein of siderite and micro-euhedral quartz (XPL). b) Sequence of siderite, galena and
55 1233 barite (PPL+ RL). c) Schematic representation of chloritoid-schist breccia cemented by various minerals (V-ore). d) Sd-
56 1234 p primary fluid inclusion in siderite. e) Brt-p in barite.

57 1235
58 1236 Figure 6: a) V-Qtz2 oblique quartz vein intersected by V-Cal oblique calcite vein. b) Relationships between V-Qtz2
59 1237 grains, Qtz2-tg and calcite vein containing Cal-p. c) Detail of Cal-p.

1 1238 Figure 7: Microthermometry and salinity data for all types of fluid inclusions from the Sierra Almagrera.

2 1239

3 1240 Figure 8: Cl/Br molar ratio vs. Cl concentration for fluid inclusions analysed both by LA-ICP-MS (empty symbols) and
 4 1241 crush-leach methods (CL, full symbols) (samples from the mining district). The seawater evaporation trend is indicated
 5 1242 (Fontes & Matray, 1993) as SW: Seawater, G: Gypsum, H: Halite, E: Epsomite, S: Sylvite, C: Carnallite, B: Bischofite.
 6 1243 Comparison data (crush-leach analysis) in boxes 1 to 4: 1—Variscan fluids equilibrated with host rocks (granite and
 7 1244 metamorphic rocks), (Boiron *et al.*, 2003), 2—Primary brines derived from Triassic evaporites in the Pyrenees (Mccaig
 8 1245 *et al.*, 2000), 3—Primary brines from Ag deposits in Morocco (Essarraj *et al.*, 2005), 4—Secondary brines associated
 9 1246 with emerald mineralization in Columbia (Banks *et al.*, 2000).

10 1247

11 1248 Figure 9: Box-and-whisker plots showing the concentrations of various elements concentrations (in ppm) in fluid
 12 1249 inclusions Qtz1-tg1, Qtz2-tg, Qtz3-p and Brt-p obtained by LA-ICP-MS method (other FI did provide significant
 13 1250 signal). Sr and Ba concentrations are not significant for Brt-p because of the presence of the element in the ablated
 14 1251 mineral matrix. Lower whiskers, bottoms of boxes, red central lines, tops of boxes and upper whiskers represent 10th,
 15 1252 25th, 50th, 75th and 90th percentiles respectively. n, number of fluid inclusions analysed, it is identical for all the
 16 1253 elements.

17 1254

18 1255 Figure 10: $\delta^{18}\text{O}_{\text{fluid}} \text{‰ V-SMOW}$ vs. $\delta\text{D}_{\text{fluid}} \text{‰ V-SMOW}$ for Qtz2-ig, Qtz3-p and Sd-p fluids. Fields of some representative
 19 1256 fluids from the literature: basinal fluids (Sheppard (1986): GC = Gulf Coast; C = California; M= Michigan).
 20 1257 Metamorphic and magmatic fluids boxes are plotted from Field and Fifarek (1985).

21 1258

22 1259 Figure 11: P (MPa) vs. T ($^{\circ}\text{C}$) of fluid inclusion stages in the Sierra Almagrera. l.p.: geothermal gradient at lithostatic
 23 1260 pressure; h.p.: geothermal gradient at hydrostatic pressure.

24 1261

25 1262 Figure 12: Exhumation of the Sierra Almagrera with associated tectonic regime, paleo-orographic evolution and
 26 1263 paleofluid sequence

27 1264

28 1265 Table 1: Abbreviations referring to microthermometric experiments.

29 1266

30 1267 Table 2: Nomenclature, location and description of sampled veins

31 1268

32 1269 Table 3: Nomenclature, chronology and characteristics of fluid inclusions. Abbreviations: -tg stands for transgranular, -
 33 1270 ig for intragranular and -p for primary, L: liquid, V: vapour, acc.: accidentally trapped mineral, Sd: siderite, Brt: barite,
 34 1271 Cal: calcite.

35 1272

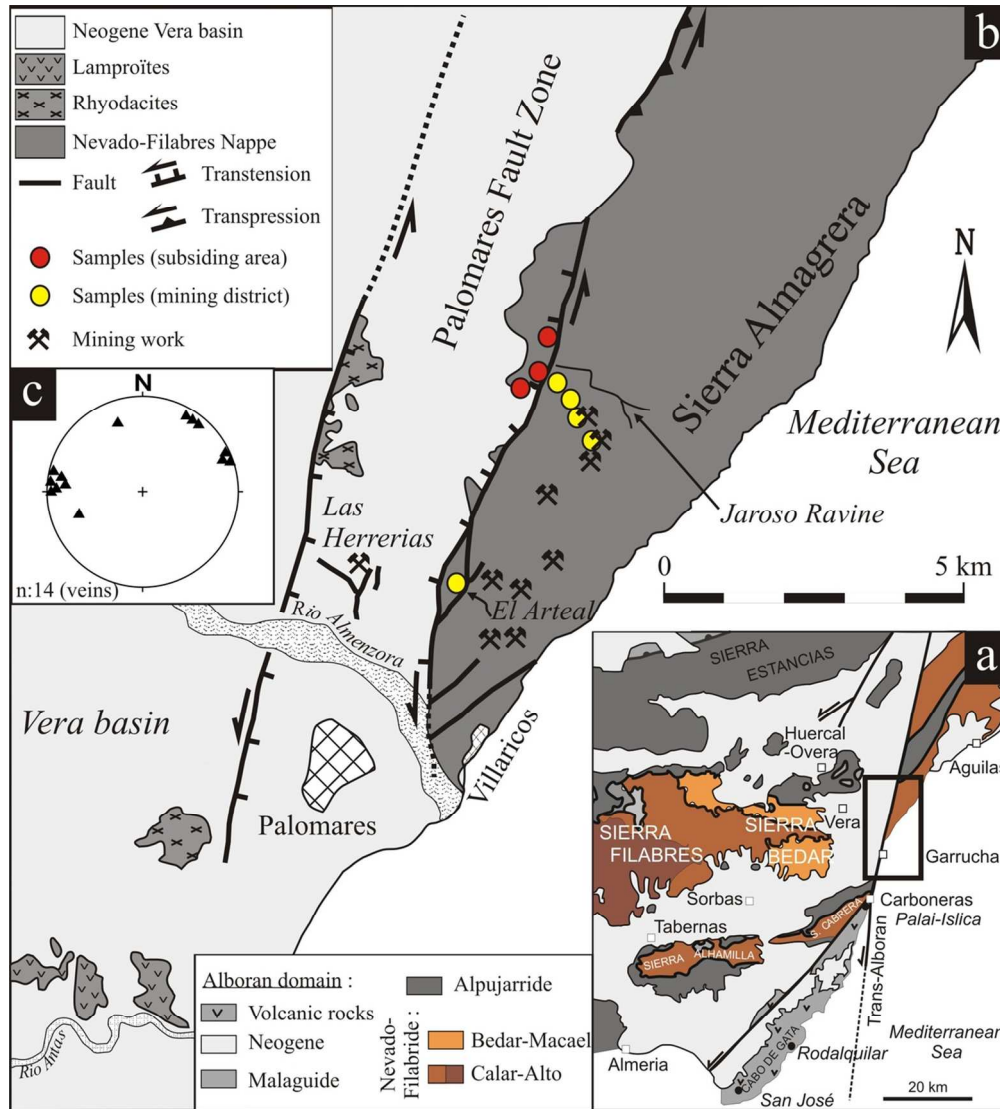
36 1273 Table 4: Microthermometric and compositional data for all generations of fluid inclusions from the Sierra Almagrera
 37 1274 (values of mode in italics). - : not determined

38 1275

39 1276 Table 5: LA-ICP-MS data for four generations of fluid inclusions from the Sierra Almagrera. Concentrations are given
 40 1277 in ppm and Na/K are mass ratios. - : not determined

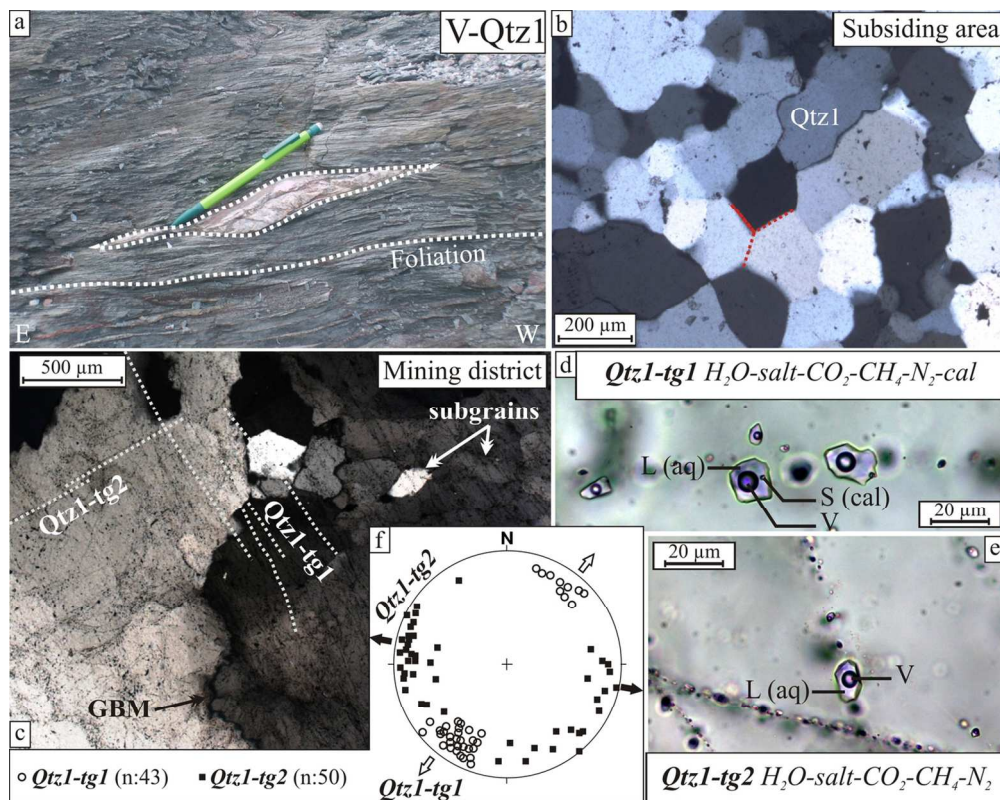
41 1278 Table 6: Isotopic data for various stages of fluid inclusions from the Sierra Almagrera, - : not determined.

42 1279



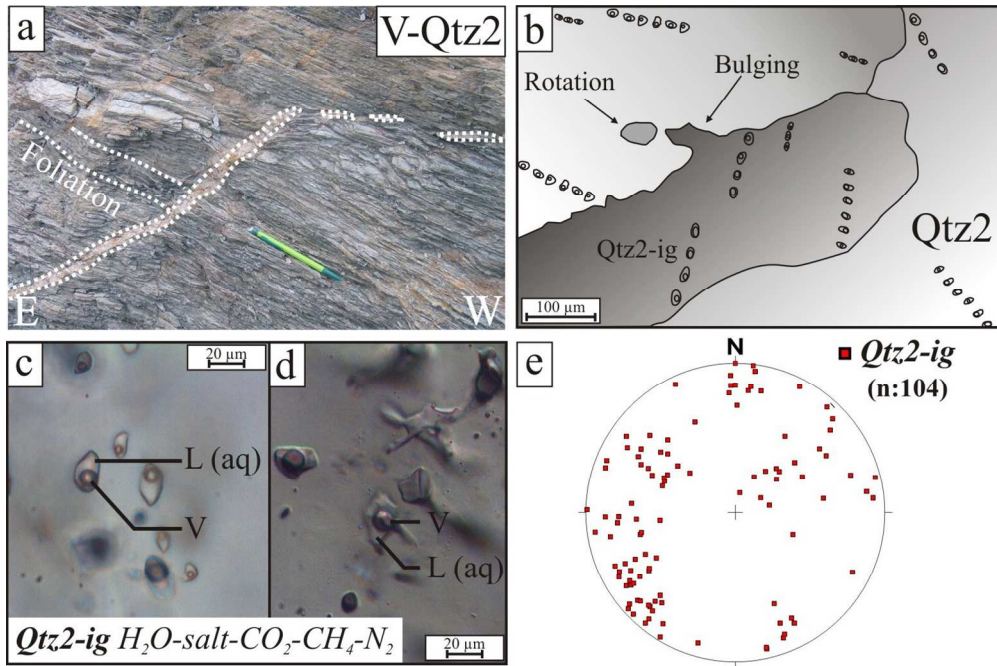
a) Geological context of the Eastern Betics and location of the Sierra Almagrera (modified after Augier (2004)). b) Geological map of the Sierra Almagrera, Vera basin and Palomares fault zone (modified after Booth-Rea (2004) and Montenat & Ott D'estevou (1990)), and location of sampling areas. c) Poles of mineralized V-ore veins (barite and siderite) in El Arteal tunnel represented on lower-hemisphere stereogram.

109x121mm (300 x 300 DPI)

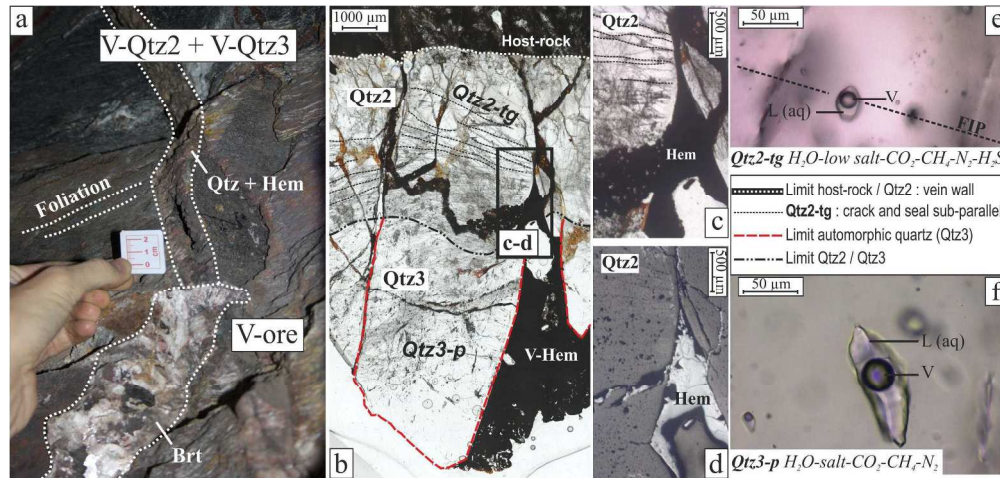


a) V-Qtz1 quartz vein parallel to the rock foliation. b) Optical microphotograph under cross-polarized light (XPL) showing petrography of Qtz1: static recrystallization (120° angles) and grain boundary migration recrystallization. c) Qtz1: recrystallised quartz with transgranular FIP. d) Qtz1-tg1 FIP. e) Qtz1-tg2 FIP. f) Pole projections of Qtz1-tg1 and Qtz1-tg2 fluid inclusion planes represented on lower hemisphere stereogram. Arrows indicate the directions of opening. L for liquid, V for vapour and S for solid.
126x100mm (300 x 300 DPI)

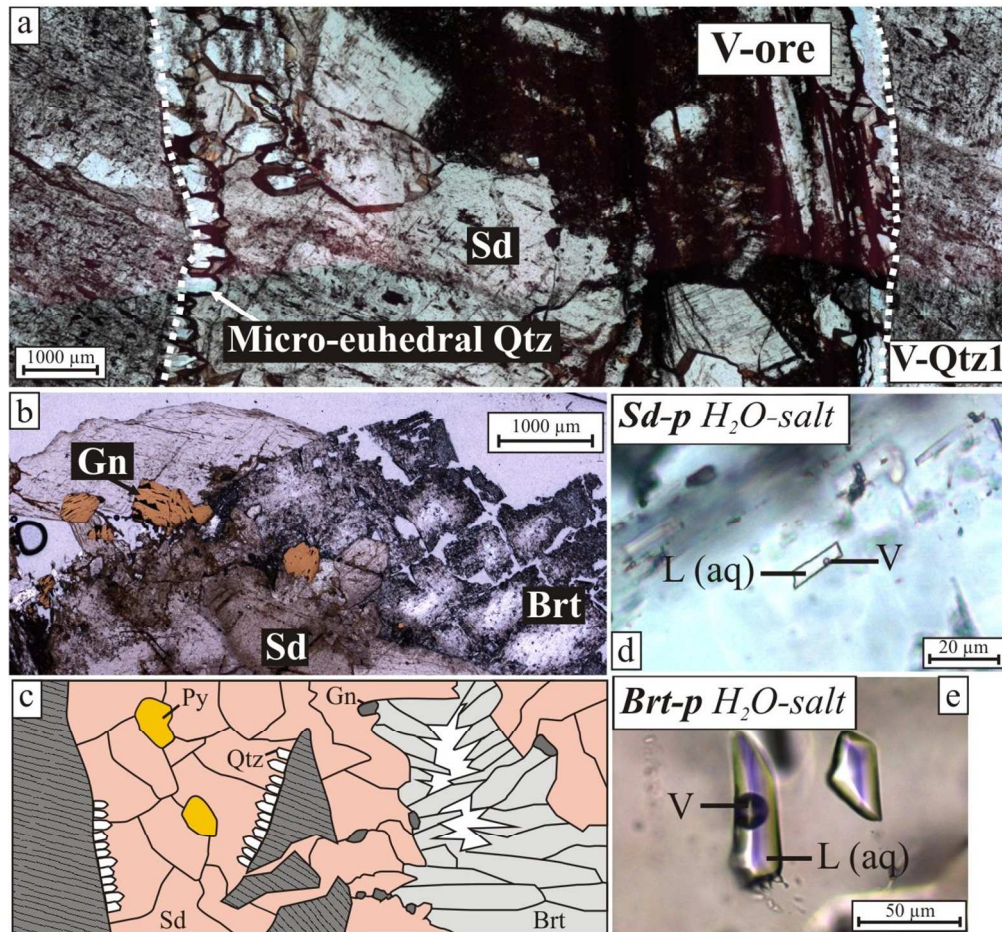
1
2
3
4
5
6
7
8
9
10
11
12
13
14
15
16
17
18
19
20
21
22
23
24
25
26
27
28
29
30
31
32
33
34
35
36
37
38
39
40
41
42
43
44
45
46
47
48
49
50
51
52
53
54
55
56
57
58
59
60



a) V-Qtz2 quartz vein locally parallel to the foliation (upper part), while the main section is discordant to the foliation (central part). b) Relationship between petrography of recrystallised quartz (subgrain rotation and bulging) and fluid inclusions. c) Optical microphotographs under plane-polarized light showing intragranular Qtz2-ig. d) Deformed fluid inclusion Qtz2-ig. e) Pole projections of Qtz2-ig fluid inclusion planes represented on lower-hemisphere stereogram.
133x88mm (300 x 300 DPI)



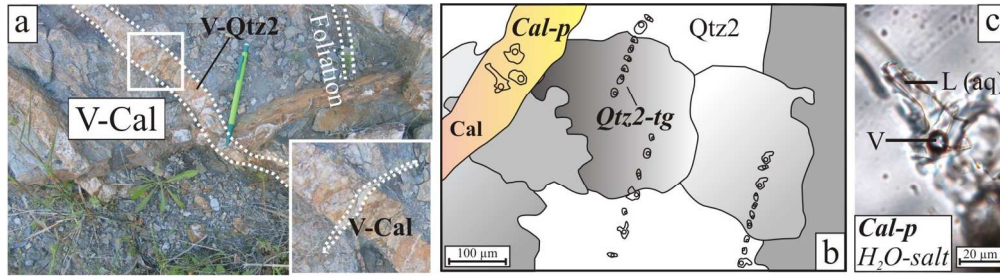
a) N10E V-Qtz2 discordant to the foliation reopened as V-Qtz3, intersected by V-ore discordant vein. Optical microphotographs under natural light: b) Contact between Qtz2 and Qtz3. Qtz2 grains still showing undulose extinction and affected by Qtz2-tg. Qtz3 euhedral quartz containing only Qtz3-p primary fluid inclusions. Hematite microfissures affecting Qtz2. Hematite also filling open spaces between Qtz3 crystals. c) Zoom of zone localized in b). d) Hematite in reflected light. e) Qtz2-tg. f) Qtz3-p. 239x113mm (300 x 300 DPI)



Optical microphotographs of V-ore and related minerals, in plane-polarized light (PPL), cross-polarized light (XPL) and reflected light (RL). a) Vein of siderite and micro-euhedral quartz (XPL). b) Sequence of siderite, galena and barite (PPL+ RL). c) Schematic representation of chloritoid-schist breccia cemented by various minerals (V-ore). d) Sd-p primary fluid inclusion in siderite. e) Brt-p in barite.

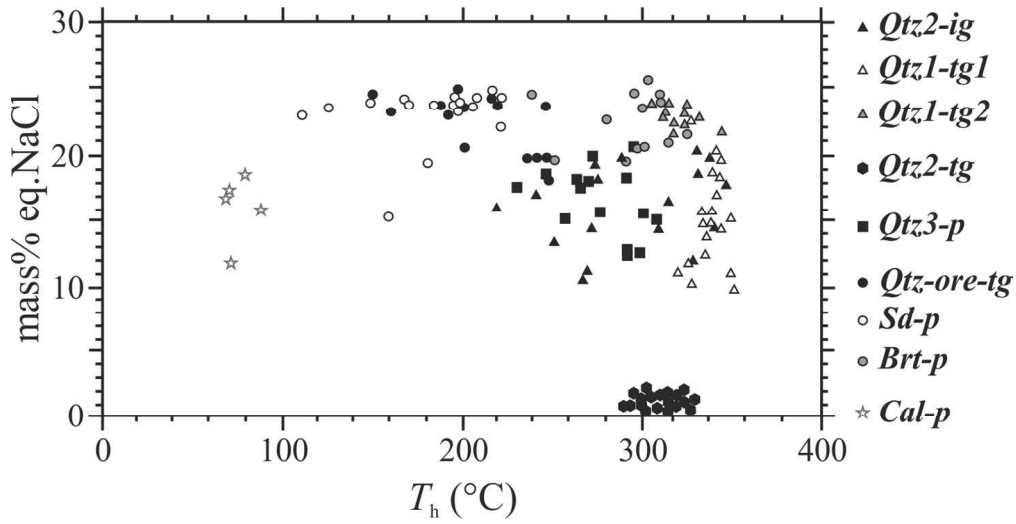
110x103mm (300 x 300 DPI)

1
2
3
4
5
6
7
8
9
10
11
12
13
14
15
16
17
18
19
20
21
22
23
24
25
26
27
28
29
30
31
32
33
34
35
36
37
38
39
40
41
42
43
44
45
46
47
48
49
50
51
52
53
54
55
56
57
58
59
60

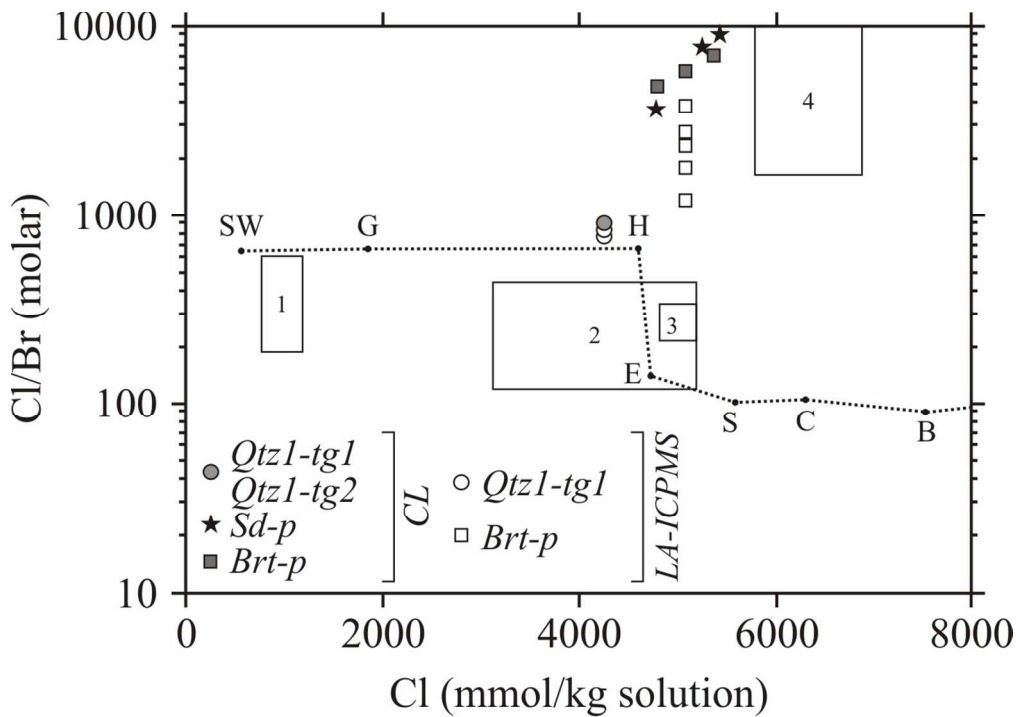


a) V-Qtz2 oblique quartz vein intersected by V-Cal oblique calcite vein. b) Relationships between V-Qtz2 grains, Qtz2-tg and calcite vein containing Cal-p. c) Detail of Cal-p.
161x44mm (300 x 300 DPI)

Draft Copy



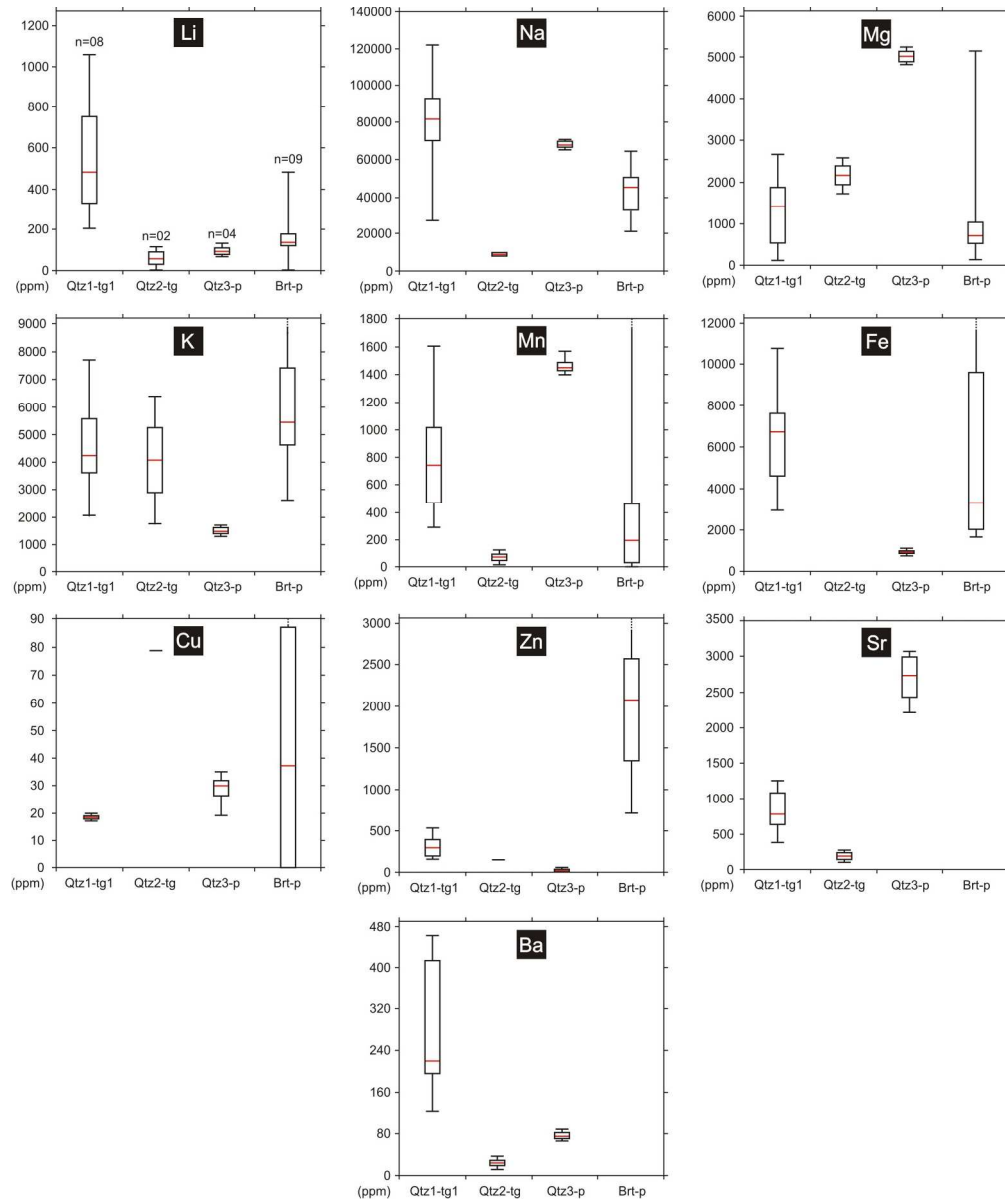
Microthermometry and salinity data for all types of fluid inclusions from the Sierra Almagrera.
124x63mm (300 x 300 DPI)



Cl/Br molar ratio vs. Cl concentration for fluid inclusions analysed both by LA-ICP-MS (empty symbols) and crush-leach methods (CL, full symbols) (samples from the mining district). The seawater evaporation trend is indicated (Fontes & Matray, 1993) as SW: Seawater, G: Gypsum, H: Halite, E: Epsomite, S: Sylvite, C: Carnallite, B: Bischofite. Comparison data (crush-leach analysis) in boxes 1 to 4: 1—Variscan fluids

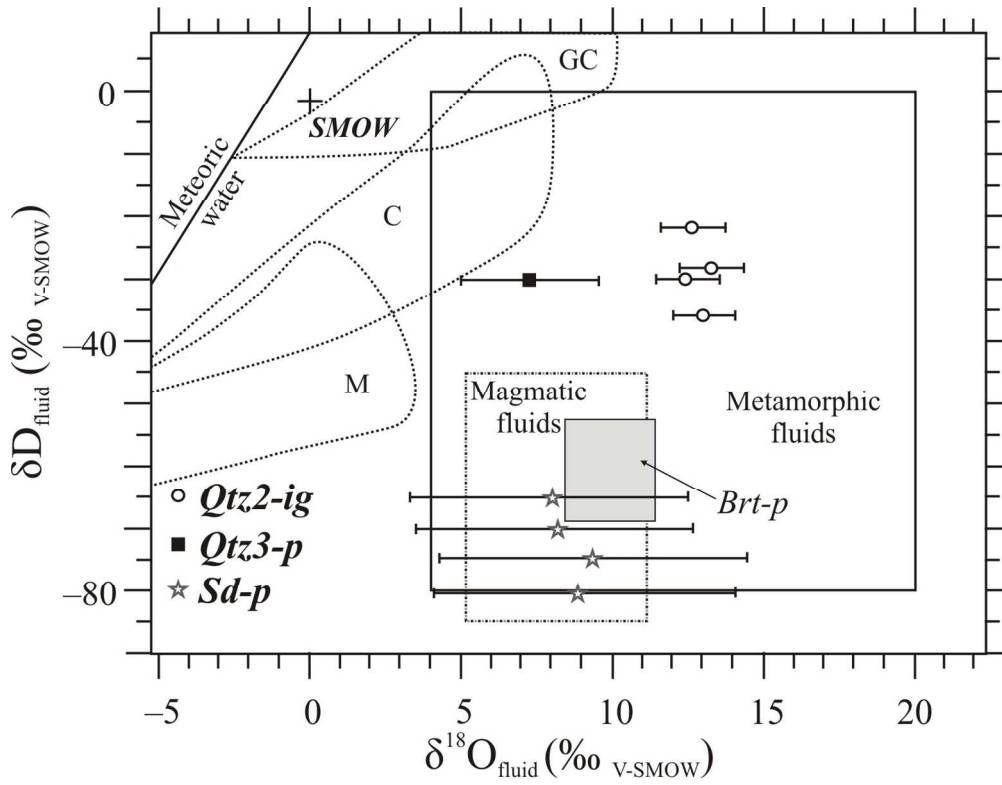
equilibrated with host rocks (granite and metamorphic rocks), (Boiron et al., 2003), 2—Primary brines derived from Triassic evaporites in the Pyrenees (Mccaig et al., 2000), 3—Primary brines from Ag deposits in Morocco (Essarraj et al., 2005), 4—Secondary brines associated with emerald mineralization in Columbia (Banks et al., 2000).

116x82mm (300 x 300 DPI)



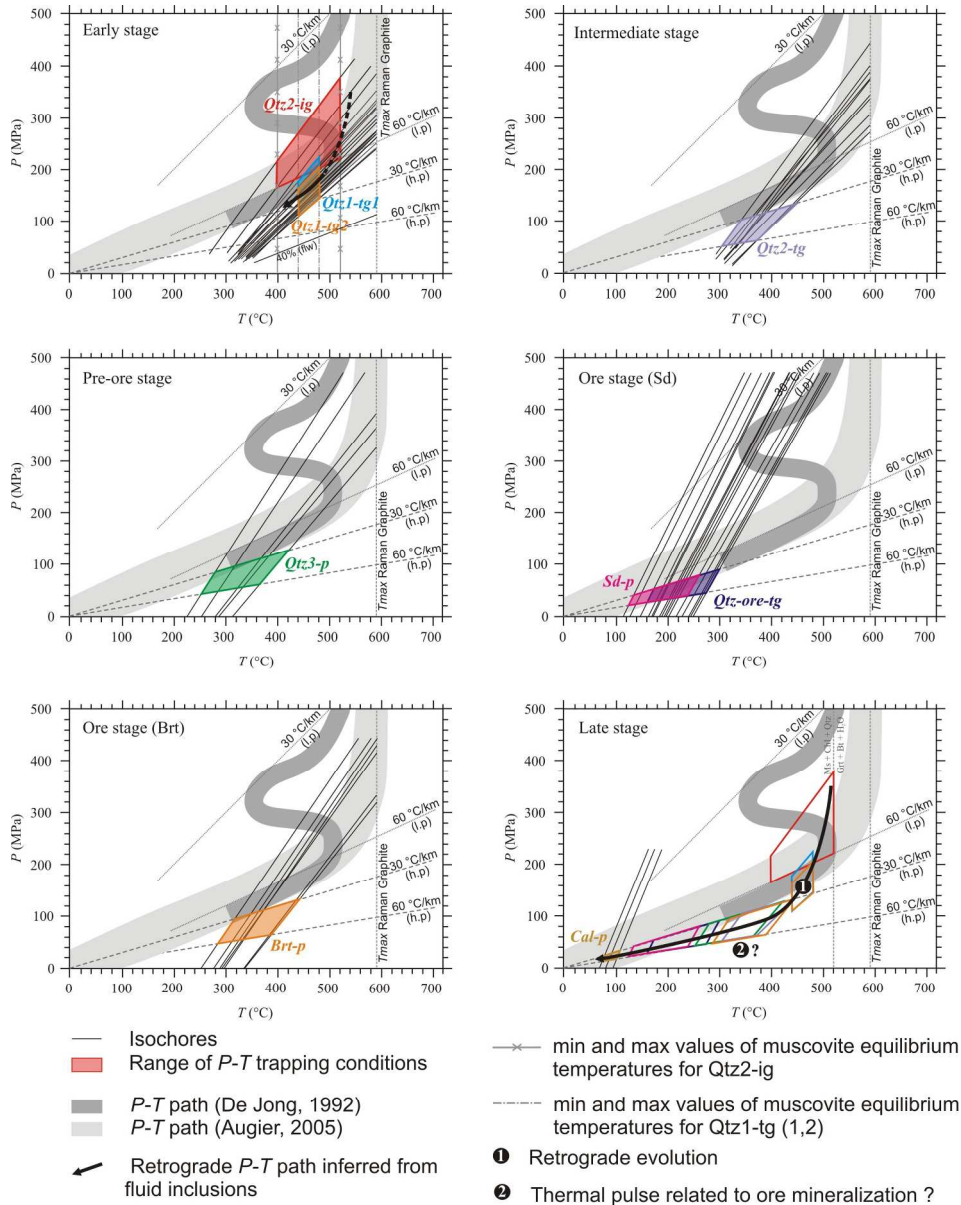
Box-and-whisker plots showing the concentrations of various elements concentrations (in ppm) in fluid inclusions Qtz1-tg1, Qtz2-tg, Qtz3-p and Brt-p obtained by LA-ICP-MS method (other FI did provide significant signal). Sr and Ba concentrations are not significant for Brt-p because of the presence of the element in the ablated mineral matrix. Lower whiskers, bottoms of boxes, red central lines, tops of boxes and upper whiskers represent 10th, 25th, 50th, 75th and 90th percentiles respectively. n, number of fluid inclusions analysed, it is identical for all the elements.

194x231mm (300 x 300 DPI)



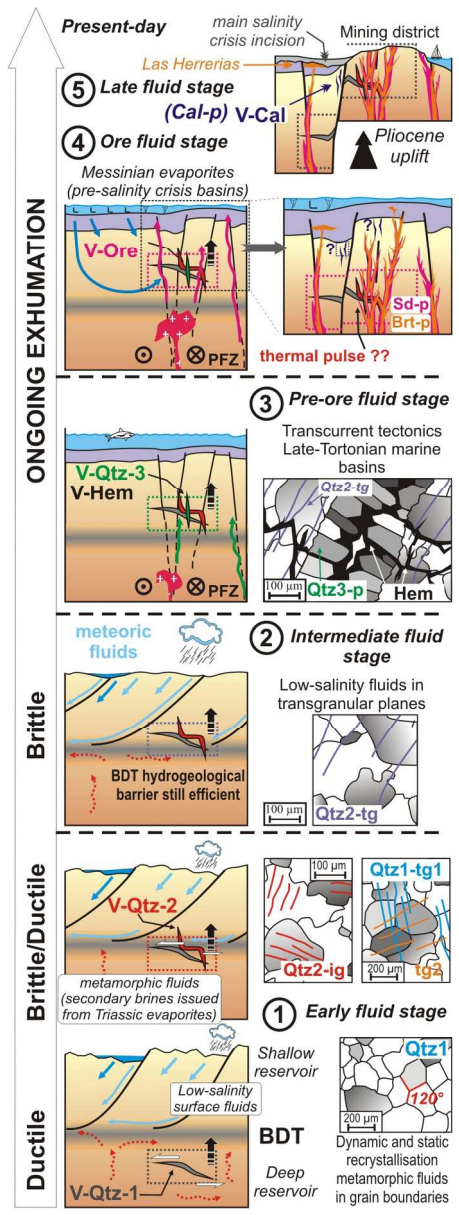
$\delta^{18}\text{O}_{\text{fluid}} \text{‰ V-SMOW}$ vs. $\delta\text{D}_{\text{fluid}} \text{‰ V-SMOW}$ for Qtz2-ig, Qtz3-p and Sd-p fluids. Fields of some representative fluids from the literature: basinal fluids (Sheppard (1986): GC = Gulf Coast; C = California; M= Michigan). Metamorphic and magmatic fluids boxes are plotted from Field and Fifarek (1985).
 146x113mm (300 x 300 DPI)

1
2
3
4
5
6
7
8
9
10
11
12
13
14
15
16
17
18
19
20
21
22
23
24
25
26
27
28
29
30
31
32
33
34
35
36
37
38
39
40
41
42
43
44
45
46
47
48
49
50
51
52
53
54
55
56
57
58
59
60



P (MPa) vs. T (°C) of fluid inclusion stages in the Sierra Almagrera. l.p.: geothermal gradient at lithostatic pressure; h.p.: geothermal gradient at hydrostatic pressure.
196x248mm (300 x 300 DPI)

1
2
3
4
5
6
7
8
9
10
11
12
13
14
15
16
17
18
19
20
21
22
23
24
25
26
27
28
29
30
31
32
33
34
35
36
37
38
39
40
41
42
43
44
45
46
47
48
49
50
51
52
53
54
55
56
57
58
59
60



Exhumation of the Sierra Almagrera with associated tectonic regime, paleo-orographic evolution and paleofluid sequence
77x208mm (300 x 300 DPI)

Abbreviation	Observation
-p	Primary fluid inclusion
-ig	Intragranular fluid inclusion plane
-tg	Transgranular fluid inclusion plane
L	Liquid
V	Vapour
S	Solid
flw	Volume fraction of aqueous liquid
T_e	Eutectic or apparent eutectic temperature. First formation of visible liquid of solid aqueous phase on heating
$T_m(\text{ice})$	Final melting temperature of solid aqueous phase
$T_m(\text{cla})$	Dissociation temperature of clathrate
$T_h(\text{L})$	Bulk homogenization temperature via bubble-point transition ($L+V=L$)
$T_h(\text{V})$	Bulk homogenization temperature via dew-point transition ($L+V=V$)

1 Table: Abbreviations referring to microthermometric experiments. .

Draft Copy

Vein type and chronology	Location	Vein / rock foliation relationships	Vein mineralogy (this study)
V-Qtz1	Subsident area	Parallel to the rock foliation	Quartz (Qtz1)
	Mining district	Parallel	Quartz (Qtz1)
V-Qtz2	Subsident area	Parallel to oblique	Quartz (Qtz2)
	Mining district	Parallel to oblique	Quartz (Qtz2)
V-Qtz3	Mining district	Oblique	Quartz (Qtz3), Hematite
V-ore	Mining district	Oblique	Quartz, Siderite, Pyrite, Galena, Barite
V-Cal	Subsident area	Oblique	Calcite

1 Table: Nomenclature, location and description of sampled veins

Draft Copy

Vein type and chronology	Fluid inclusion petrography	Strike direction	Size (µm)	Shape	Filling	Flw (vol %)
V-Qtz1	-	Grain boundary	?		?	?
	Qtz1-tg1	N130°	~20	Equant, rounded Euhedral	L, V, acc. calcite	65-75 65-75
	Qtz1-tg2	N000° - N030°	15-25		L, V	
V-Qtz2	Qtz2-ig	Random	15-25	Euhedral to dismembered	L, V	50-80
	Qtz2-tg	N000° - N010°	10-15	Equant, rounded	L, V	70-80
V-Qtz3	Qtz3-p	Primary inclusions	>50	Elongated	L, V	70-75
V-ore	Qtz-ore-tg	N000° - N010°	5-10	Euhedral	L, V	70-90
	Sd-p	Primary (cleavage planes)	5-20	Euhedral, flat	L, V	70-90
	Brt-p	Primary (cleavage planes)	30-50	Euhedral, irregular	L or L, V	65-80
V-Cal	Cal-p	Isolated clusters	20-70	Irregular, flat	?	80-95

Table: Nomenclature, chronology and characteristics of fluid inclusions. Abbreviations: -tg stands for transgranular, -ig for intragranular and -p for primary, L: liquid, V: vapour, acc.: accidentally trapped mineral, Sd: siderite, Brt: barite, Cal: calcite.

Draft Copy

Fluid inclusion petrography	Fluid inclusion type	Microthermometry					Calculated composition						
		T_e (°C)	$T_m(\text{Ice})$ (°C)	$T_m(\text{Cla})$ (°C)	T_h (°C)	Salinity (mass% eq. NaCl)	V_m (cm ³ /mol)	H ₂ O (mol %)	CO ₂ (mol %)	CH ₄ (mol %)	N ₂ (mol %)	H ₂ S (mol %)	NaCl (mol %)
Qtz1-tg1	Aqueous carbonic	-48.6/-39.8 <i>-45.2</i>	-22.7/-7.7 <i>-14.5</i>	-3.8/6.5 <i>6.0</i>	319/350 <i>330</i>	9.7/22.6 <i>15.0</i>	23.1/29.2 <i>27.2</i>	85.2/88.1 <i>87.0</i>	1.9/3.6 <i>2.8</i>	0.01/0.1 <i>0.08</i>	0.01/0.05 <i>0.03</i>	-	9.5/11.3 <i>10.1</i>
Qtz1-tg2	Aqueous carbonic	-64.6/-39.8 <i>-55.1</i>	-23.1/- <i>17.6</i>	-5.7/-2.3 <i>-3.2</i>	305/344 <i>320</i>	21.6/23.8 <i>23.0</i>	22.8/25.6 <i>23.4</i>	80.7/84.2 <i>81.0</i>	2.8/5.2 <i>3.3</i>	0.01/0.3 <i>0.1</i>	0.01/0.06 <i>0.04</i>	-	12.3/16.4 <i>15.6</i>
Qtz2-ig	Aqueous carbonic	-45.7/-30.9 <i>-35.0</i>	-20.0/-8.4 <i>-16.0</i>	-2.5/-1.1 <i>-2.1</i>	220/355 <i>340</i>	11.9/20.6 <i>17.0</i>	25.3/30.0 <i>27.1</i>	82.3/89.1 <i>85.0</i>	2.4/5.6 <i>3.0</i>	0.01/0.3 <i>0.2</i>	0.01/0.07 <i>0.02</i>	-	10.1/12.8 <i>11.8</i>
Qtz2-tg	Aqueous carbonic	-	-3.0/-0.7 <i>-1.5</i>	7.3/12.3 <i>9.8</i>	290/330 <i>300</i>	0.1/2.4 <i>1.2</i>	20.5/27.0 <i>25.3</i>	92.3/96.2 <i>95.0</i>	2.5/4.1 <i>3.0</i>	0.01/0.2 <i>0.1</i>	0.05/0.3 <i>0.1</i>	0.03/0.07 <i>0.05</i>	0.1/2.5 <i>1.8</i>
Qtz3-p	Aqueous carbonic	-	-21.7/-9.0 <i>-17.3</i>	-2.7/-1.2 <i>-1.8</i>	189/308 <i>265</i>	12.7/20.9 <i>18.3</i>	20.7/23.0 <i>22.6</i>	89.2/94.1 <i>91.0</i>	1.2/3.2 <i>2.5</i>	0.01/0.1 <i>0.05</i>	0.01/0.06 <i>0.04</i>	-	5.2/8.8 <i>6.4</i>
Qtz-ore-tg	Aqueous	-49.6/-39.6 <i>-45.0</i>	-24.3/-14.7 <i>-21.2</i>	-	150/248 <i>210</i>	18.4/25 <i>23</i>	19.6/21.5 <i>20.5</i>	83.0/87.0 <i>85.0</i>	-	Trace	-	-	13.0/17.0 <i>15.0</i>
Sd-p	Aqueous	-49.0/-40.1 <i>-44.3</i>	-23.5/-11.4 <i>-23.2</i>	-	110/222 <i>190</i>	15.4/24.6 <i>24.1</i>	18.8/20.9 <i>19.4</i>	80.3/85.6 <i>83.0</i>	-	Trace	-	-	15.2/18.3 <i>17.0</i>
Brt-p	Aqueous	-59.1/-41.6 <i>-56.2</i>	-25.3/-17.7 <i>-22.4</i>	-	237/335 <i>305</i>	20.7/25.8 <i>23.0</i>	21.0/24.0 <i>23.0</i>	80.1/84.6 <i>82.0</i>	Trace	Trace	Trace	-	12.3/19.2 <i>18.0</i>
Cal-p	Aqueous	-	-15.0/-8.0 <i>-14.0</i>	-	67/87 <i>80</i>	11.8/18.4 <i>17.0</i>	18.6/18.9 <i>18.7</i>	87.2/89.1 <i>88.0</i>	-	-	-	-	10.4/13.1 <i>12.0</i>

Table: Microthermometric and compositional data for all generations of fluid inclusions from the Sierra Almagrera (values of mode in italics). - : not determined

1
2
3
4
5
6
7
8
9
10
11
12
13
14
15
16
17
18
19
20
21
22
23
24
25
26
27
28
29
30
31
32
33
34
35
36
37
38
39
40
41
42
43
44
45
46
47
48
49

Fluid inclusion name	Li	Na	Mg	K	Mn	Fe	Cu	Zn	Sr	Ba	Na/K
Qtz1-tg1	1060	91098	1418	4407	1605	8376	-	523	1028	461	21
	328	69786	-	2936	400	2919	-	193	378	122	24
	543	90418	108	4994	748	5074	-	177	603	217	18
	325	70319	1444	7660	1021	6339	17	479	790	414	9
	202	27260	844	2043	285	7412	20	169	734	222	13
	750	122326	199	3847	730	7102	-	276	1217	215	32
	782	98756	2660	7222	1010	10758	-	360	1240	414	14
	569	73880	2274	3999	489	3161	-	286	641	136	18
Qtz2-tg	0	8198	1719	6347	18	-	-	-	268	13	1
	115	9551	2592	1734	122	-	80	135	104	35	6
Qtz3-p	118	69072	5173	1462	1442	953	31	21	3068	87	47
	126	68540	5236	1326	1563	1028	35	35	2958	80	52
	120	70210	4852	1652	1402	1032	19	15	2500	70	43
	145	67500	4956	1420	1453	856	29	42	2201	68	48
Brt-p	280	47306	1044	7522	310	2093	621	2075	-	-	6
	-	31792	5162	4613	10530	25082	-	4758	-	-	7
	483	63865	1379	6187	329	4438	-	1328	-	-	10
	121	64455	675	9458	842	1660	-	702	-	-	7
	176	45509	1005	4805	-	-	74	1858	-	-	9
	134	34292	511	3698	7	-	32	2124	-	-	9
	169	50607	704	5396	71	-	37	1341	-	-	9
	72	32586	444	7389	-	-	232	2688	-	-	4
125	21303	121	2629	36	-	94	2577	-	-	8	

1 Table: LA-ICP-MS data for four generations of fluid inclusions from the Sierra Almagrera. Concentrations are given in ppm and Na/K are mass ratios. - : not determined

Vein type	Fluid inclusion petrography	$\delta^{18}\text{O}_{\text{host}}$ (V-SMOW ‰) min - max (<i>n</i>) <i>median</i>	$T_{\text{trapping}}^{(1)}$ (°C)	$\delta^{18}\text{O}_{\text{fluid}}^{(2)}$ (V-SMOW ‰) min - max <i>median</i>	$\delta\text{D}_{\text{fluid}}$ (V-SMOW ‰) min to max (<i>n</i>) <i>median</i>	$T_{\text{equilibrium}}^{(3)}$ min to max (°C)
V-Qtz1	Grain boundary	16.5 - 16.7 (2) 16.6	-	-	-33 to -36 (2) -34.5	488 - 520
V-Qtz1	Qtz1-tg1+tg2	15.9 - 17.2 (2) 16.6	440 - 480	-	-28 to -30 (2) -29.0	442 - 478
V-Qtz2	Qtz2-ig	16.2 - 17.0 (4) 16.5	400 - 520	11.7 - 14.2 12.8	-23 to -36 (4) -30.0	404 - 520
V-Qtz2	Qtz2-tg	15.9 - 17.6 (7) 16.6	300 - 560	-	-17 to -48 (7) -34.0	365 - 704
V-Qtz3	Qtz3-p	14.0 - 14.5 (2) 14.3	250 - 380	5.0 - 9.6 7.4	-30 (1) -30	459
V-ore	Sd-p	20.6 - 22.5 (4) 21.5	120 - 260	3.2 - 14.5 8.8	-65 to -80 (4) -71.5	> 1630
V-ore	Brp-p	13.0 - 13.2 (2) 13.1	280 - 440	8.2 - 11.3 9.7	-53 to -69 (7) -58.0	831 - 1025

⁽¹⁾ Obtained from isochore intersection with PT-path

⁽²⁾ Equation of Zheng (1993) for quartz-H₂O fractionation; equation of Zheng (1999) for siderite-H₂O and barite-H₂O fractionation

⁽³⁾ Equation of Suzuoki and Epstein (1976) for muscovite-H₂O fractionation between $\delta\text{D}_{\text{fluid}}$ and $\delta\text{D}_{\text{host-rock}} = -52\text{‰}$

Table: Isotopic data for various stages of fluid inclusions from the Sierra Almagrera, - : not determined.